

REPORT DOCUMENTATION PAGE

0423

Public reporting burden for this collection of information is estimated to average 1 hour per response, including the time for reviewing instructions, data needed, and completing and reviewing this collection of information. Send comments regarding this burden estimate or any other aspect of this burden to Department of Defense, Washington Headquarters Services, Directorate for Information Operations and Reports (0704-0188), 1215 Jefferson Davis Highway, Suite 1204, Arlington, VA 22202-4302. Respondents should be aware that notwithstanding any other provision of law, no person shall be subject to any penalty for failing to comply with a collection of information if it does not display a currently valid OMB control number. PLEASE DO NOT RETURN YOUR FORM TO THE ABOVE ADDRESS.

1. REPORT DATE 17-Sep-2003	2. REPORT TYPE Final Technical Report	3. DATES COVERED (From - To) 01-Apr-2001 to 30-Jul-2003		
4. TITLE AND SUBTITLE Fundamental Studies of Microstructure Evolution during Stir Welding of Aluminum Alloys		5a. CONTRACT NUMBER		
		5b. GRANT NUMBER F49620-01-1-0300		
		5c. PROGRAM ELEMENT NUMBER		
6. AUTHOR(S) P.R. Subramanian, Nirm V. Nirmalan, Lisa M. Young, Paul Sudkamp, David P. Mika, Michael Larsen, Michelle A. Othon, Paul L. Dupree, Sarah O. Walker, Gregory M. Catlin		5d. PROJECT NUMBER		
		5e. TASK NUMBER		
		5f. WORK UNIT NUMBER		
7. PERFORMING ORGANIZATION NAME(S) AND ADDRESS(ES) General Electric Company GE Global Research Center P.O. Box 8 Schenectady, NY 12301		8. PERFORMING ORGANIZATION REPORT NUMBER		
9. SPONSORING / MONITORING AGENCY NAME(S) AND ADDRESS(ES) USAF, AFRL AF Office of Scientific Research 801 N. Randolph St., Rm. 732 Arlington, VA 22203-1977		AFOSR/PK4		
		11. SPONSOR/MONITOR'S REPORT NUMBER(S)		
12. DISTRIBUTION / AVAILABILITY STATEMENT Distribution Statement A. Approved for public release; distribution is unlimited.				
13. SUPPLEMENTARY NOTES				
14. ABSTRACT This research program was aimed at developing a fundamental understanding of microstructural evolution in FSW Al alloys. The microstructural evolution in FSW-processed alloys is closely connected to the local thermomechanical cycles imposed through the combination of frictional heating and mechanical working by the tool material. The mechanical and corrosion properties of the resultant joints, in turn, are intimately linked to the evolved microstructures. In an effort to understand these relationships, FSW simulations were conducted on monolithic Al 6061 and Al 2195 plates. Thermal fields produced during FSW were determined using infrared (IR) imaging and embedded thermocouples. Efforts have been made to establish the link between the thermal fields and the resultant microstructural evolution in the various FSW zones. Texture evolution in the FSW zones has been evaluated using electron backscatter diffraction (EBSD). The influence of microstructural features on tensile, fatigue, and corrosion behavior is presented.				
15. SUBJECT TERMS Friction Stir Welding; Al 2195 alloys; Thermal Imaging; Microstructural Evolution, Corrosion; Fatigue; Texture				
16. SECURITY CLASSIFICATION OF: Unclassified		17. LIMITATION OF ABSTRACT UU	18. NUMBER OF PAGES 58	19a. NAME OF RESPONSIBLE PERSON P. R. Subramanian
				19b. TELEPHONE NUMBER (include area code) (518) 387-6154
a. REPORT	b. ABSTRACT	c. THIS PAGE		

20031028 177

GE Global Research

Technical Report Abstract Page

Title FUNDAMENTAL STUDIES OF MICROSTRUCTURAL EVOLUTION DURING
FRICTION STIR WELDING OF ALUMINUM ALLOYS

Principal Investigator:

P. R. Subramanian*

Phone 518 387-6154

Contributors:

Nirm V. Nirmalan[^]

Lisa M. Young**

Paul Sudkamp (currently at GE Aircraft Engines)

David P. Mika[#]

Michael Larsen↑

Michelle A. Othon↑

Paul L. Dupree*

Sarah O. Walker[^]

Gregory M. Catlin*

Component *Ceramic & Metallurgy Technologies; [^]Energy & Propulsion Technologies; [#]Inspection & Manufacturing Technologies; ↑Biosciences, Combichemistry, & Characterization Technologies

Abstract

This research program was aimed at developing a fundamental understanding of microstructural evolution in FSW Al alloys. The microstructural evolution in FSW-processed alloys is closely connected to the local thermomechanical cycles imposed through the combination of frictional heating and mechanical working by the tool material. The mechanical and corrosion properties of the resultant joints, in turn, are intimately linked to the evolved microstructures. In an effort to understand these relationships, FSW simulations were conducted on monolithic Al 6061 and Al 2195 plates. Thermal fields produced during FSW were determined using infrared (IR) imaging and embedded thermocouples. Efforts have been made to establish the link between the thermal fields and the resultant microstructural evolution in the various FSW zones. Texture evolution in the FSW zones has been evaluated using electron backscatter diffraction (EBSD). The influence of microstructural features on tensile, fatigue, and corrosion behavior is presented.

**Formerly at GE – Global Research Center, Schenectady, NY.

FUNDAMENTAL STUDIES OF MICROSTRUCTURAL EVOLUTION DURING FRICTION STIR WELDING OF ALUMINUM ALLOYS

TABLE OF CONTENTS

EXECUTIVE SUMMARY	3
BACKGROUND	4
Friction Stir Weldng	4
FSW Structures	5
FSW of Aluminum Alloys	6
Mechanical Behavior Studies	7
Corrosion Studies	9
In situ Temperature Measurement Techniques	10
RESEARCH OBJECTIVES	10
EXPERIMENTAL	11
RESULTS AND DISCUSSIONS.....	13
Thermal Measurements.....	13
Microstructural Observations	14
SEM Studies	14
TEM Studies	16
EBS Analysis & Texture Evolution	17
Room-Temperature Tensile Behavior	18
Corrosion Behavior	18
Fatigue Behavior	20

CONCLUSIONS.....	21
RECOMMENDATION FOR FUTURE WORK	22
ACKNOWLEDGMENT	23
REFERENCES.....	23

EXECUTIVE SUMMARY

Friction stir welding (FSW) is an enabling solid-state joining process for fabrication of low-cost lightweight structures. Substantial efforts are under way in the development of this technology for fabrication of large structures, such as airframes and cryogenic tanks for space applications. Concepts such as unitization (i.e., reduction of rivets and joints) in aerospace structures are attractive candidates for reducing weight and cost. Friction stir welding is one of the processes under development as an enabling joining technique for fabrication of affordable unitized structures. While all of these technology developments are occurring at a good pace, at the fundamental level there is a clear need for a comprehensive understanding of the microstructural transformations occurring during the process, as these microstructural changes control the long-term integrity of the welded joint.

This research program was aimed at developing a fundamental understanding of microstructural evolution in FSW Al alloys. The microstructural evolution in FSW-processed alloys is closely connected to the local thermomechanical cycles imposed through the combination of frictional heating and mechanical working by the tool material. The mechanical and corrosion properties of the resultant joints, in turn, are intimately linked to the evolved microstructures. In an effort to understand these relationships, FSW simulations were conducted on monolithic Al 6061 and Al 2195 plates. Thermal fields produced during FSW were determined using infrared (IR) imaging and embedded thermocouples. Efforts have been made to establish the link between the thermal fields and the resultant microstructural evolution in the various FSW zones. Texture evolution in the FSW zones has been evaluated using electron backscatter diffraction (EBSD). The influence of microstructural features on tensile, fatigue, and corrosion behavior is presented.

BACKGROUND

Friction Stir Welding

Friction stir welding is an innovative joining process that was invented at The Welding Institute in the United Kingdom in 1991 [1]. It is an essentially solid state process that involves rotating a non-consumable cylindrical tool at high speeds (a few hundred rpm), plunging it into a rigidly clamped workpiece, followed by traversal along the joint to be welded [Figure 1]. The welding tool is specially designed to provide a combination of frictional heat and thermomechanical working to accomplish the weld. Typically, the cylindrical tool consists of a large-diameter shoulder region with a smaller diameter entry pin. The rotating entry pin contacts the workpiece surface and rapidly provides frictional heating, thus softening a region of the metal. The rotational contact of the larger diameter shoulder creates additional frictional heat and plasticizes a cylindrical metal column around the inserted pin. As the rotating tool tracks the weld interface, it provides a continuous thermomechanical working action, plasticizing metal within a narrow zone while extruding metal from the leading face of the pin to the trailing edge. The moving column of stirred hot metal consumes the weld interface, thus providing a strong solid-state joint in the wake of the tool [2]. Process parameters such as FSW tool rotation speed, plunge rate/force, and tool traversal rates along the weld joint are specific to the alloys that been welded to date and have been extensively investigated; these details will not be discussed here. Similarly, weld tool design issues are also beyond the scope of this background discussion.

The distinguishing characteristics of this process are—

- Solid-state nature of the process, thus circumventing solidification-induced problems such as cracking or porosity that are inherent in conventional fusion welding processes;
- Fine hot-worked microstructure compared to a typically dendritic structure in conventional fusion joints;
- Potential ability to join difficult-to-weld alloys;
- Lower heat input to the workpiece with attendant reduction in residual stresses and part distortion, thereby reducing costs by eliminating straightening steps in fabrication;
- Absence of the need for surface preparation and removal of surface oxides;
- Absence of need for filler material, again offering the potential for cost reduction;
- Process flexibility and scalability to weld large scale structures as well as thick sections;

- Environmentally clean process with no major safety hazards, i.e., welding fumes or radiation
- Absence of need for a protective environment, especially when such welds are performed in space;

Additionally, the process offers the possibility of obtaining improved mechanical properties compared to conventional fusion welds, with higher joint strengths, increased weld joint ductility, and improved fracture characteristics. The process has been demonstrated to have great potential for joining difficult-to-weld aluminum alloys [3-6]. It is being developed by Lockheed-Martin to replace a low-productivity fusion welding process for joining the space shuttle external tanks [3].

FSW Structures

To date, friction stir welding has been successfully demonstrated only for solid-state joining of non-weldable Al-alloys [4-6]. Substantial work has been performed on developing process parameters for robust FSW of several Al-alloys. Several studies have characterized the microstructures developed in the weld zone as well as in the weld-base metal interface. Gradients in the level of solid-state deformation and temperature associated with FSW may generate a continuous spectrum of microstructural changes. These changes include, but are not limited to, diffusional and diffusionless phase transformations, grain refinement, coarsening, and recrystallization. Each of these effects can significantly alter the microstructures, thereby changing the properties of the materials in and near the weld line. The friction-stir welds are characterized by well-defined weld nuggets and material flow contours, which are mostly oval in shape. Typically, the following zones have been observed [6-8]:

- Dynamically recrystallized zone (DXZ). In this region commonly referred to as the weld nugget or the stir zone (SZ), the high temperatures and high levels of deformation result in full dynamic recrystallization and the formation of a fine-grain equiaxed microstructure. The weld nugget is roughly the same size as the tool pin that penetrates the workpiece. The dynamically recrystallized zone is indicative of hot-working produced by the combination of heat induced by the rotating tool as well as the forging action produced by the shoulder of the tool as it traverses along the joint. This is in contrast to a fusion-welded joint, which shows a dendritic structure representative of a solidification process. The formation of the dislocation structure and the recovery and recrystallization behavior in this region during FSW are not well understood.

- Thermomechanically affected zone (TMZ). In this region, the deformation is sufficient to cause grain reorientation and rotation; however, the grains are not recrystallized. Depending on the particular alloy considered, this region might reach temperatures where recovery of the deformed structure occurs and precipitates are coarsened or dissolved. Understanding the microstructural development due to deformation, phase transitions, and precipitate coarsening will ultimately determine the mechanical and fatigue properties of the material.
- Heat-affected zone (HAZ). A well-defined HAZ is present in heat-treatable alloys; this zone is adjacent to the TMZ. In this zone, only thermal effects are present; no deformation structures are expected. If precipitates are present, the distribution of precipitates throughout the interior of the metal grains remains homogeneous. However, the thermal excursion may result in a coarsened precipitate structure and growth of intergranular precipitates. If the alloy considered does not contain precipitates, the microstructural changes will depend on the stability of the starting alloy and could result in additional phase transformations or a tempered microstructure.
- Reheated surface zone. This region is associated with the surface deformation and surface recrystallization caused by the rotating tool shoulder. It should be emphasized that further microstructural details are specific to the type of alloy investigated, and these will be described in detail below.

FSW of Aluminum Alloys

Microstructures developed in FSW have been characterized in detail for several aluminum alloys [8-22]. The salient features are summarized in Table 1. The overall observations are that in most cases the temperatures generated in the FSW zone exceeded the precipitate solvus temperatures. As a result, precipitate dissolution and re-precipitation has been noted in specific alloys. Also, the re-precipitation appeared to occur with random orientation, and in some cases, the precipitates were overaged. In all likelihood, the temper heat treatment imparted to the original rolled aluminum plates is destroyed during FSW. As a result, the original microstructure of the workpiece is not retained in the final FSW zone. Fragmentation or break-up of strengthening particles was also observed in some of the alloys. These observations suggest a clear need for a

comprehensive understanding of the thermal fields produced during FSW and their subsequent linkage to microstructures as well as properties.

Mechanical Behavior Studies

Microhardness profiles across the FSW zones [9-10,12-14,16, 18,20] showed trends that were specific to the alloys being investigated. In cast, as well as cold-rolled Al 1100, no significant variations in hardness were observed between the weld zones and the base metal [9-10].

Hardness trends in Al 6061 [12-14] indicated a significant softening in the weld zone, which was explained on the basis of a reduction in the dislocation density caused by dynamic recrystallization [12]. From the weld zone to the base metal, there is a continuous variation in the microhardness, which correlates spatially with the variations in precipitation structures and crystallographic distributions in the different regions [13]. A small drop in the hardness in the HAZ has been associated with over-aging effects[14]. Svensson and Karlsson [18] noticed a significant reduction in hardness in the weld zone in Al 6082, which they have correlated with the absence of hardening precipitates and Guinier-Preston (GP) zones in the weld nugget. The hardness of the weld nuggets in Al 2014 and Al 7075 [16] was observed to be higher than that of the base metal; this was attributed to increased solid solution strengthening arising from the dissolution of the age-hardening precipitates during friction stir welding. The HAZ region in these alloys showed the lowest hardness value. This was explained as being due to the weakening of the grains in the HAZ by over-aging of the precipitates (eta phase) and loss of solute to the coarse precipitate materials. Hardness profiles on friction stir welded Al 7050 [20] showed an increase in hardness in the weld nugget that has been attributed to contributions from the fine grain size as well as the high dislocation density observed in some of the grains. The HAZ region showed a decrease in hardness arising from the coarsening of the precipitates in this region.

Tensile tests of the weld nugget in Al 7075 in the longitudinal direction showed no loss of ductility, but strength reductions were observed that were attributed to the reduction in preexisting dislocations and dissolution of the fine hardening precipitates [8]. The fracture surface of the as-welded alloy showed the presence of fine microvoids at grain surfaces; the intergranular failure was associated with the coalescence of these microvoids. Post-weld thermal aging significantly restored the tensile strength through re-formation of the fine hardening precipitates, but there was a loss in ductility. Tensile tests of friction stir welded Al 7075 in the

transverse direction showed loss of both strength and ductility. However, in contrast to the longitudinal tests, failure in the transverse tests occurred by shear fracture in the HAZ well away from the weld nugget [8], thereby indicating softening due to thermal effects. Tensile data on friction stir welded Al 7050 [20] indicated an overall decrease in ductility by ~60%; post-weld heat treatments only partially restored the ductility. Lienert and Grylls [14] reported tensile properties in friction stir welded Al 6061 that were about 30–45% lower than those of the base metal, with failure occurring in the HAZ. They noted that the temperature excursions in the HAZ were sufficiently large to cause coarsening of the precipitates with attendant decrease in strength. It is clear from all of these studies that a detailed analysis of the microstructural effects is needed to fully understand the mechanical behavior of the friction stir welded materials.

Crack resistance measurements in friction stir welded Al 2024 showed a substantial increase in fracture toughness compared to the base metal [17]. This increase was related to the presence of smaller and rounder particles in the weld metal that nucleated voids at high loads, whereas the base metal had large primary particles that nucleated voids at fairly low loads and therefore showed low fracture toughness.

Bussu and Irving [23] performed constant amplitude fatigue tests on both longitudinal and transverse butt joints of friction stir welded Al 2024. In both cases, the fatigue performance was inferior to that of the base metal, although the longitudinal orientations showed a better fatigue life compared to the transverse orientations. Fatigue initiation sites correlated well with the minimum hardness sites in the welds, thereby indicating that the softening caused by FSW can degrade the fatigue performance of these materials. The fatigue behavior of the friction stir welded specimens was also influenced by the weld surface conditions; removal of stress-concentrating features by surface skimming brought the fatigue strength to within 90% of the base metal fatigue strength. Biallas et al. [17] did not notice any significant loss in fatigue strength of friction stir welded Al 2024, but thick sections showed a loss in high-cycle fatigue strength essentially resulting from the notch effect of the weld. Fatigue crack growth experiments were conducted on friction stir welded Al 7050 [20] to evaluate the fatigue characteristics of the weld nugget region as well as the HAZ region. Their results showed the weld nugget to have inferior fatigue crack growth resistance, with no clear indication of the mechanisms of fatigue

failure. On the other hand, the fatigue crack growth resistance of the HAZ was better than that of the parent metal. This has been attributed to compressive residual stresses generated in the HAZ that induced significant crack closure.

Corrosion Studies

Corrosion studies on FSW 2195 alloys have been conducted by Li et al. [21], Hu and Meletis [24], and Corral et al. [25]. Slow-strain rate (SSR) tests [21,23] on specimens pre-exposed to a 3.5% NaCl solution indicated that the base metal has a higher stress corrosion cracking (SCC) susceptibility compared to FSW Al 2195. SCC of these alloys is primarily associated with the T₁ phase (Al₂CuLi). This platelet-like phase is very active in a 3.5% NaCl solution; consequently, the dissolution of these platelets results in an increased susceptibility to environmental-assisted cracking. TEM examination [21] of the FSW AL 2195 weld nugget suggested that the T₁ phase was completely dissolved. Thus, FSW Al 2195 was expected to be less susceptible to SCC than the parent metal. Anodic polarization measurements by Corral et al. [25] showed FSW and base metal Al 2195 to have nearly identical corrosion potentials.

Biallas et al. [17] studied the stress-corrosion cracking behavior of FSW Al 2024 by four-point bend testing in an aqueous 3% NaCl solution. Intergranular corrosion and pitting were observed in the fine-grained weld nugget. Immersion tests showed exfoliation corrosion attack in the thermomechanically-affected zone next to the weld. These results were supported by corrosion potential measurements across the weld, thereby indicating that the cause of corrosion was primarily related to galvanic effects resulting from the microstructural variations.

Lumsden et al. [26] used slow strain rate tests in 3.5% NaCl solution as well as immersion tests to assess the stress corrosion susceptibility of Al 7050. The as-welded Al 7050 (in the T7451 temper condition) was shown to be susceptible to stress-corrosion attack, with intergranular fracture concentrated in the transition zone between the weld nugget and the thermomechanically affected zone. A post-weld artificial aging treatment almost completely restored the stress corrosion resistance. This suggests that any debit in corrosion properties in the friction stir welded material may be addressed through appropriate post-weld treatments.

In-situ Temperature Measurement Techniques

Feng et al. [27] have related the temperature evolution during friction stir welding to three key process variables: rotation speed, downward plunge force, and traverse rate. Temperatures generated during the process have been monitored by in-situ thermocouple measurements [28-31] and infrared imaging [32]. A brief description of the state-of-the-art regarding infrared (IR) measurement is included here. With the development of fast, high-resolution IR imaging systems, IR thermography has been used successfully for nondestructive inspections, evaluations, and quality assurance of airfoils used in gas turbines [33-35]. Many commercially available IR imaging systems support excellent temperature precision for either fast frame rates or for small spatial resolutions. However, it is difficult to achieve temperature precision with both short temporal and fine spatial resolutions. Presently, the thermal imaging systems with high spatial and thermal resolution capability (600 x 800 pixels and 0.1C) tend to be relatively slow at capturing data, at about 8–10 frames/s. This type of camera has been used to take steady-state thermal data for fundamental research and to evaluate turbine blade cooling strategies [36-38]. One of these high-resolution cameras has been used extensively to take steady-state data on airfoil cooling designs on flat-plate geometry [33]. Transient IR imaging systems have been developed and are currently in use at GE for nondestructive evaluation of material, bonds, and surface treatments in gas turbine blades, as well as for direct heat transfer measurements in turbomachinery [35]. Transient methodology that relies on complete characterization of the absolute temperatures of the imaged surface is documented by Stiglich et al. [34].

RESEARCH OBJECTIVES

The friction stir welding process comprises hot-working produced by the combination of heat induced by the rotating tool as well the forging action produced by the shoulder of the tool as it traverses along the joint. Therefore, the microstructural evolution in friction stir welding of aluminum alloys is closely connected to the thermomechanical cycles locally imposed on the various zones. The microstructural development can be best understood by evaluating hot-working parameters, such as strain, strain rate, and temperatures generated during the welding process, which in turn are related to process variables inherent in the friction stir welding process.

The objectives of this research program were as follows:

- Development of an accurate profile of the thermal fields produced during friction stir welding by careful temperature measurements using a combination of infrared imaging and embedded thermocouples, and coupling these measurements with the observed weld microstructures as well as mechanical properties;
- Detailed analysis of the microstructural features developed in the various FSW zones, using scanning electron microscopy (SEM) and transmission electron microscopy (TEM) studies, and relating the microstructural development to the thermal field evaluation results;
- Experimental investigation of tensile and fatigue properties as a function of local microstructural modifications within the weld zone;
- Characterization of the corrosion behavior of the FSW alloys and relating this behavior to the microstructural features unique to the process.

The outcome of these research activities is a fundamental understanding of how thermal fields produced during friction stir welding influences microstructural evolution in FSW joints, and in turn, how the variations in the microstructures influence the tensile, fatigue, and corrosion properties of the FSW joint.

EXPERIMENTAL

An Al-Li based alloy (Al 2195) was selected for establishing the methodology proposed in this effort. The nominal composition of Al 2195 is as follows: 4.3Cu; 1.41Li; 0.03Si, 0.05Fe, 0.35Mg, 0.01Ni, 0.02Zn; 0.02Ti; 0.4Ag; 0.13Zr; balance Al (compositions in weight percent). This alloy has been employed for the fabrication of lightweight external tanks for the Space Shuttle. This alloy is also the most likely candidate for next-generation space applications.

A horizontal milling machine was specially adapted for the FSW trials. This machine allows for rigid clamping of the workpiece plates during the FSW run. FSW pin tools were fabricated from H-13 steel bar stock. The initial objective of this effort was to develop an accurate profile of the thermal fields produced during FSW by careful temperature measurements using a combination of infrared (IR) imaging and embedded thermocouples. Initial calibration trials were completed

using instrumented plates of Al 6061. Surface temperatures on the top (tool side) of the work-piece were measured primarily using a transient IR imaging system with high spatial and thermal resolution capability. The thermal images were obtained using a high-resolution IR camera at a high rate of 60 frames/second, thereby capturing the evolving thermal profile during FSW. Temperatures within the work-piece were measured using arrays of thermocouples embedded in the work-piece at different longitudinal and transverse locations. An array of 15 thermocouples attached to the bottom of a 15" long x 4" wide x 0.375" thick work-piece was used for temperature measurements at specific locations. Additionally, several thermocouples were surface-mounted along the FSW joint and at selected locations on either side at a distance of 1" from the joint. These thermocouples also allowed for calibration of the transient infra-red (IR) imaging system during the FSW runs. The combination of infrared and thermocouple measurement techniques served to provide a complete description of the plate temperature history during tool plunging as well as during tool traversal along the weld joint.

The friction stir welding process was simulated in monolithic Al plates by traversing the rotating tool along the work-piece so that a welded zone is obtained on the trailing side of the tool. This is convenient for evaluating the microstructures generated by the process rather than evaluating the joint quality. Evaluations of weld parameters and tool design were not important objectives in this study. The optimum parameters for FSW were selected based on the literature, together with data obtained from internal GE studies. Reasonable parameters for friction stir welding of aluminum alloys are in the range 400–500 rpm for rotation rates and 1–2 mm/s for translation rates. In this study, two different tool rotation rates (214 and 430 RPM) were employed to evaluate the effect of varying heat input on FSW microstructures. A typical run consisted of plunging the rotating tool into the workpiece, and following a dwell time of ~10 seconds, traversing the rotating tool along the workpiece at a rate of ~ 2 mm/second (4.25 inches/minute). Figure 2 (a) shows a FSW run in progress on the instrumented Al 6061 plate, while Figure 2 (b) shows one of the FSW experiments on an Al 2195 plate. In Fig. 2(a), the thermocouples in line with the weld joint record the maximum temperature at the point when the tool shoulder comes in contact with the thermocouple tip. Figure 3 shows the plates that were subjected to the initial bead-on-plate runs.

RESULTS AND DISCUSSIONS

Thermal Measurements

The temperature profiles generated at the underside of the Al 6061 plate as well as along the joint line during the FSW tool plunge and during tool traversal are plotted in Figures 4 (a) and (b).

During the tool plunge, a maximum temperature of 460-480°C was observed directly under the rotating FSW pin, and the temperature decay was fairly rapid following the tool traversal along the plate. The peak temperatures in Figure 4(b) represent the temperatures at the weld line at the pin shoulder-workpiece contact point (the thermocouples get destroyed once the shoulder traverses past the thermocouple tip). These peak temperatures are of the order of 460-480°C.

Figures 5 (a) and (b) show the temperature profiles obtained from the top of the plate at locations 25 mm (1") to the left as well as right of the joint line [location of thermocouples on the trailing edge (TE) and leading edge (LE) is shown in Fig. 5(c)]. In these locations, the temperatures reached a maximum of 265-285°C on the trailing edge (TE) and 275-300°C on the leading edge (LE) of the joint line, thereby indicating that the leading edge has a slightly higher temperature than the trailing edge of the weld joint. These data are consistent with the observations reported by other investigators. The data also shows that the temperature decay is quite rapid away from the joint line. This observation has important implications in the resultant microstructural evolution in the weld nugget and adjacent zones.

Following the initial evaluations, bead-on-plate FSW simulations were conducted on 12.7 mm (0.5") thick Al 2195 plates. Two different tool rotation speeds (214 and 430 RPM) were employed to vary the heat input to the "stir" region during FSW. The tool traversal rate was kept constant at 2 mm/sec (4.25 inches/min). High-speed IR thermal images were obtained from the regions in the vicinity of the rotating tool during the FSW of AA2195. Figure 6 shows a still thermal image from one of the IR frames. The thermal images were used to extract discrete temperature data from selected locations along the weld joint as well as normal to the weld joint from the thermal images [Figs. 7(a) and 7(b)]. The axial and lateral temperature profiles taken at fixed locations from the FSW tool's frame of reference showed a rapid drop-off in temperature away from the tool-workpiece interface, thereby indicating that temperature rise during tool plunging and traversal is fairly local to the weld joint.

Temperature profiles in-line with the FSW joint were also obtained using an array of embedded and surface-mounted thermocouples at both the backside and the top of the workpiece. The temperature profiles in-line with the traversing tool are compared as a function of time for the two different tool rotating speeds (214 and 430 RPM) in Figure 8. Thermocouples were located at distances of 50 mm (2"), 100 mm (4"), 150 mm (6"), and 200 mm (8") from the start of the weld. Again, the maximum temperature corresponds to the point where the tool shoulder comes in contact with the thermocouple. The maximum temperatures at the tool shoulder-workpiece contact points are ~460-490°C for the 214-RPM weld and ~500-520°C for the 430-RPM weld. Figure 9 shows the temperature profiles as a function of time at the bottom of the workpiece in-line with the traversing tool for the two different rotation speeds. The maximum temperatures here correspond to the instance when the rotating tool is plunged into the workpiece or when the tool passes the thermocouple. In general, the maximum temperatures under the tool were generally 20-30°C higher for the 430-RPM weld. Further, higher heating rates during the tool plunge were recorded for the 430-RPM weld. These results can be explained on the basis of the higher frictional heat generated by the higher tool rotation speed, thus resulting in higher metal temperatures and higher heating rates.

Figures 10 (a) and (b) show the temperature profiles obtained from the top of the Al 2195 plate at locations 25 mm (1") to the left as well as right of the joint line [along TE and LE as shown in Fig. 10(c)]. In these locations, the leading edge consistently showed a slightly higher temperature than the trailing edge of the weld joint (~15°C for the 214-RPM and ~35°C for the 430-RPM weld).

Microstructural Observations

SEM Studies

SEM examination of the as-FSW-processed joints (Figure 11) for the 2 different weld speeds revealed the three distinct microstructural zones that are typical of FSW material: (1) a dynamically recrystallized, fine grain, equiaxed structure (DXZ) in the weld nugget; in contrast, the parent metal showed highly elongated and pancake-shaped grain structures, which is typical of rolled Al-alloy microstructures; (2) a thermo-mechanically affected zone (TMZ) on either side of the DXZ zone, where the deformation was sufficient to cause significant grain reorientation

and rotation, but not recrystallization, and (3) a heat-affected zone (HAZ) adjacent to the TMZ zone, where only thermal effects are present with no deformation expected. The asymmetry in the FSW processed region across the centerline of the joint is typical of friction stir-welded structures, and is a consequence of the movement of plasticized material around the rotating pin tool during tool translation along the joint. Visualization studies of material flow in Al 2195 FSW by Seidel and Reynolds [39] showed different flow patterns on the leading edge (or advancing side) and trailing edge (or retreating side) of the joint.

Figures 12 and 13 show details of the microstructures within each of the different FSW zones for the 214- and 430-RPM tool rotation speeds, respectively. The tool rotation speeds have a direct influence in the frictional heat input to the FSW process zones. This is manifested in different thermal exposures in the different FSW zones, which in turn, influences the microstructural evolution in each of those zones. In the weld nugget, the maximum temperatures during FSW are in the range ~460-490°C for the 214-RPM weld and ~500-520°C for the 430-RPM weld. The workpiece in this region has thus been subjected to high temperatures and high strain rates indicative of severe thermomechanical working. Consequently, this region has a fully recrystallized, fine-grained microstructure. Figure 14 (a) shows such a microstructure within the DXZ region, while Fig. 14 (b) shows the transition zone from the DXZ region to the thermo-mechanically affected zone (TMZ) and the HAZ region. In Fig. 14(b), grain re-orientation and rotation are clearly visible in the transition region. Thus, the FSW process results in the replacement of the elongated grains in the original parent metal with a fine, equiaxed grain structure in the weld nugget. According to Jata and Semiatin [40], the FSW process causes the metal in the DXZ region to undergo dynamic recrystallization through a continuous process, in a manner similar to the microstructural evolution observed in hot deformed structures. This similarity with hot worked structures was inferred from the relation between the sub-grain size in the weld nugget and the Zener-Holloman parameter [$Z = \dot{\varepsilon} \cdot e^{[Q/RT]}$], where $\dot{\varepsilon}$ is the deformation strain rate, Q is the activation energy of the deformation process, and T is the deformation temperature. Using values of $Q=190$ kJ/mol and $\dot{\varepsilon}=10$ s⁻¹ from Jata and Semiatin [40], and measured temperature profile within the weld nugget and sub-grain size from this study, the resultant value of inverse grain size vs. Log(Z) is close to the data calculated by Jata and Semiatin, and this in turn, is in close accord to the trend measured on hot worked Al-Li

structures. The process of dynamic recrystallization within the weld nugget has been reported to be via dislocation glide-assisted sub-grain rotation, resulting in a high degree of misorientation. The grain sizes within the weld nugget in the 430 RPM FSW specimen were ~25% larger than those in the 214 RPM specimen, as illustrated in Figs. 15 (a) and (b) for the center of the weld nugget, and in Figs. 15(c) and (d) for regions within the DXZ close to the TMZ. This is qualitatively in accord with the temperature observations for the two different speeds. The higher temperatures in the material processed at 430 RPM presumably led to more grain growth.

TEM Studies

Oertelt et al. [22] have predicted the equilibrium phases precipitating in Al 2195 as a function of temperature based on thermodynamic calculations. The measured temperatures during FSW are compared with the predicted phase equilibria in Figure 16. The results suggest that some of the equilibrium precipitates such as Al_3Zr and Al_2CuMg may undergo dissolution at the temperatures encountered during FSW. Transmission electron microscope (TEM) images of precipitates in the DXZ region of the as-FSW 214-RPM specimen are shown in Figure 17. $\text{Al}_7\text{Cu}_4\text{Li}$ or T_B precipitates were observed in both grain boundary and transgranular locations (Figs. 17(a) and (b)). A low density of fine spherical particles was also observed within the grains [Fig. 17(c)]. Electron diffraction showed superlattice reflections consistent with a $\text{L}1_2$ structure, indicating that these particles may be β' - Al_3Zr or $\text{Al}_3(\text{Zr},\text{Li})$, although Oertelt et al. [22] did not detect β' - Al_3Zr precipitates in the DXZ region. Weak streaks along [100] directions in the diffraction pattern suggest the presence of GP zones. These results are consistent with the TEM studies conducted by Li et al. [21] on FSW-processed Al 2195 alloys. Additionally, ~100 nm long needle-like precipitates with a morphology similar to that reported for the T_1 or Al_2CuLi phase [22] were observed at scattered locations (Fig. 17d). EDS analysis showed this needle-like phase to be enriched in Cu compared to the matrix; however the chemistry of this phase could not be identified. However, Li et al. [21] had reported the absence of T_1 precipitates in their FSW-processed alloys. The difference between Li's results and the present observations may be related to the kinetics of phase transformations, which in turn, may be influenced by FSW parameters such as tool speed and tool traversal rate.

EBS Analysis & Texture Evolution

Electron-beam scattering (EBS) analysis was performed on the as-FSW specimen to determine texture evolution within the various FSW microstructural zones. The initial results indicated a weak $<100>$ fiber texture within the thermo-mechanically affected zone (TMZ), while the texture was marginal in the equiaxed DXZ region within the weld nugget. This is in contrast to the strong $<111>$ deformation texture observed in the base metal.

A representative sample cut from the FSW plate was used for more detailed EBS analysis. The analysis was performed on a face normal to the tool path direction. Figure 18 shows the resultant Euler map of the left side of the weld and part of the base metal. The map encompasses the base metal region of very elongated grains on the left transitioning to a region of rotated base metal grains, through the HAZ and to the weld nugget on the right with equiaxed grains. Here, the color mapping corresponds to crystallographic orientation. Black pixels are areas where the orientation quality was too low to determine orientation, most likely to occur on grain boundaries, but also possible within the grains. Figure 19 shows a detailed image of the base metal region shown in Fig. 18. The pole figures for the base metal region are also shown in Fig. 19; a total of 32986 grains were used in the sample to give a texture peak of 11.78. The texture is unique in that it does not correspond to an expected rolling texture that would be expected for the base metal material. This texture may be due to a unique processing of the Al plate in the as-received condition, possibly due to cross rolling.

Figure 20 shows the Euler map and pole figures for the transition region (shown in Fig. 18) from base metal to TMZ/HAZ regions. This area includes the TMZ region where the base metal grains are rotated by their proximity to the stir zone. The gross rotation of base metal material is reflected in the pole figure rotation, while changes within the HAZ are diffusing the peaks in the texture, which have dropped to 6.47 from the 11.78 of the base material.

The Euler map and pole figures for the weld-nugget are shown in Figure 21. Here, the grains are equiaxed and have the most random texture at 2.19 and 5.21 for zones on the left and right of the nugget zone, respectively.

Room-Temperature Tensile Behavior

Room temperature tensile tests were performed on as-FSW Al 2195 in the longitudinal (all-weld metal) as well as transverse orientations to the joint. Figure 22 shows the specimens configurations relative to the FSW joint. In all of the transverse specimens, the FSW region was located in the gage section of the tensile specimens. The longitudinal (all-weld metal) tensile specimens were machined from the different zones of the FSW joint on either side of the weld-centerline. Figure 23 compares the transverse tensile data for the 214- vs. 430-RPM specimens with parent metal data from Li et al. [21] and FSW 2195 data from Arbegast et al. [41]. The transverse tensile strengths for both the 214- and 430-RPM FSW specimens are comparable to the data from Arbegast et al. [41], although the overall properties of the FSW material are inferior to those of the parent Al 2195 metal. The failure strains for the 430-RPM FSW specimens were about 30% lower than those for the 214-RPM specimens, although their strengths were similar. The two 430-RPM specimens failed in the TMAZ region [Fig. 24 (a)], while the 214-RPM specimens failed either within the HAZ region or within the base metal [Fig. 24 (b)].

Tensile test specimens for the all-weld metal properties (longitudinal orientation) were extracted from the weld nugget region. The test data are summarized in Fig. 25, where the individual data are taken from specimens on either side of the joint centerline. All-weld metal tensile strengths for 214- and 430-RPM specimens are similar-but lower than the parent Al 2195 metal. The 214-RPM processed welds showed a ductility of over 25% in the weld nugget as well as in the adjacent zone. On the other hand, 430-RPM weld showed a distinctly lower ductility in the weld nugget region. The all-weld properties were nearly symmetrical on either side of the weld-nugget centerline.

Corrosion Behavior

The corrosion behavior of the FSW weld nugget is expected to be different from corrosion in the base metal, and this may affect the long-term structural integrity of the FSW material. Specifically, the microstructural variations in the different FSW zones are expected to produce galvanic effects that may induce localized corrosion, such as pitting. SCC of Al-Li type alloys is primarily associated with the T_1 phase (Al_2CuLi). This platelet-like phase is very active in a 3.5% NaCl solution; consequently, the dissolution of these platelets during FSW may result in a

decreased susceptibility to stress corrosion cracking. Since the FSW microstructure is unique, it is reasonable to test the SCC resistance via generally accepted testing methods. Under such conditions, the slow-strain rate (SSR) test is a good screening tool for investigating the resistance of materials to environmentally assisted cracking.

The influence of friction stir welding on SCC behavior was evaluated using smooth round tensile bars under constant increasing stroke (10^{-6} in/sec), corresponding to a strain rate equal to 10^{-6} sec⁻¹ for the 1 inch specimen gage, during exposure to room temperature 3.5% NaCl solution. A pre-exposure of 4 hours in aqueous 3% H₂O₂ + 3.5% NaCl solution was used for the gage section of each bar to encourage pit formation. Pits have often been observed as SCC initiation sites in Al alloys, during the ensuing strain-to-failure in aqueous 3.5% NaCl exposure. Test parameters were determined by recommendations in [42] and [43]. All specimens were obtained from the 214-RPM weld material.

Tensile strength data [Fig. 26(a)] indicate an increased SCC susceptibility for the weld materials compared to parent Al 2195 material, with a slightly larger reduction for the transverse (T) orientation compared to the longitudinal (L) orientation (13% vs. 9%, respectively). These results are in contrast to the literature data [21,23] which indicated that the base metal has a higher stress corrosion cracking (SCC) susceptibility compared to FSW Al 2195. It is speculated that the increased susceptibility for the weld metal as observed in our study may be attributed to the presence of the active T₁ phase within the weld nugget. On the other hand, the TEM results of Li et al. [21] on FSW Al 2195 weld nugget suggested the complete absence of the T₁ phase, which supports their observation of decreased susceptibility to SCC within the weld metal. The difference between Li's results and the present observations may be related to the kinetics of T₁ dissolution, which in turn, may be influenced by FSW parameters such as tool speed and tool traversal rate.

Comparison of the % elongation results between air and aqueous NaCl environment shown in Figure 26 (b) also shows susceptibility to SCC for each of the materials, but to slightly different degrees than that shown by the tensile strength data. Note that the base metal results in Figures 26 (a) and 26 (b) were obtained from the transverse orientation in the wrought plate; it is expected that this orientation will have lower % elongation than the longitudinal (rolling

direction) in the base metal (base metal specimens in the longitudinal orientation were not available for this study). Future work should focus on the effect of post weld heat treatment on susceptibility to SCC in both the longitudinal and transverse directions; it has been reported that post weld heat treatment improves SCC resistance in welded Al 7050 [26]. This improvement in SCC resistance is likely related to the general observation that SCC resistance increases as the alloy progresses from underaged to peak aged to overaged condition. A detailed understanding of the SCC mechanisms to include effects such as, for example, change of the electrochemical potential of the precipitates with overaging, changes in hydrogen trapping behavior, as well as grain boundary segregation profiles changes, was beyond the scope of this investigation.

Fatigue Behavior

Extensive fatigue characterization was not within the original scope of this investigation. In this study, limited fatigue crack growth tests were conducted using notched compact tension specimens. Jata et al. [20] have indicated that the crack growth behavior of cracks parallel to the weld-path is dependent on the location of the crack in the weld region. Thus, in order to determine the role of the weld microstructure on fatigue crack growth behavior, the compact tension specimens were fabricated with notches placed at the different weld zones, namely, within the weld nugget and the HAZ regions (Fig. 27). Specimens were also obtained from the base metal. The specimens were ~0.25 in thick and ~0.8 in wide, with a starting notch length of 0.16 in. The tests were conducted in laboratory air at a frequency of 10 Hz with a stress ratio(R) = 0.1. The electric potential drop method was used to monitor the crack growth during the tests; an optical microscope was used to validate the crack length measurements.

Fatigue crack growth rates (da/dN) versus cyclic stress intensity (ΔK) in the HAZ and weld nugget regions are compared with the data for the base metal in Figure 28. The base metal was seen to experience heavy crack arrest/ crack growth redirection in part due to the transversely oriented grains relative to the crack growth direction. The behavior in the weld nugget was seen to be very reproducible. On the other hand, the HAZ region exhibited periods of crack arrest and rapid advancement.

The $da/dN - \Delta K$ relationships can be represented by the Paris equation as follows:

Base metal: $\frac{da}{dN} = 2 \times 10^{-10} \Delta K^{4.063}$

HAZ $\frac{da}{dN} = 1 \times 10^{-9} \Delta K^{3.635}$

Weld nugget: $\frac{da}{dN} = 2 \times 10^{-9} \Delta K^{3.620}$

The crack growth rates in the Paris law regime for the HAZ and weld nugget zones were slightly slower than the rate for the base metal. Similar results were observed by John and Jata [44] for the fatigue crack growth behavior of HAZ vs. parent metal in FSW Al 7050. The fatigue thresholds for the HAZ and weld nugget zones are similar, and appear to be slightly lower than the threshold for the base metal, although the data are rather sparse near the fatigue threshold regime. More detailed studies are required to delineate the fatigue threshold behavior of the different FSW microstructural zones.

CONCLUSIONS

- (1) Measurement of temperature profiles during FSW indicated that the maximum temperatures at the tool shoulder-workpiece contact points are $\sim 460\text{-}490^\circ\text{C}$ for the 214-RPM weld and $\sim 500\text{-}520^\circ\text{C}$ for the 430-RPM weld. This is attributed to the higher frictional heat generated by the higher tool rotation speed, thus resulting in higher metal temperatures and higher heating rates.
- (2) The FSW-processed joints for the 2 different weld speeds revealed the three distinct microstructural zones that are typical of FSW material: a dynamically recrystallized, fine grain, equiaxed structure (DXZ) in the weld nugget; a thermo-mechanically affected zone (TMZ) on either side of the DXZ zone, and a heat-affected zone (HAZ) adjacent to the TMZ zone.
- (3) The grain sizes within the weld nugget in the 430 RPM FSW specimen were $\sim 25\%$ larger than those in the 214 RPM specimen. This is qualitatively in accord with the higher temperatures observed in the material processed at 430 RPM, which presumably led to more grain growth.

(4) TEM of the DXZ region of the as-FSW 214-RPM showed $\text{Al}_7\text{Cu}_4\text{Li}$ (T_B) precipitates in both grain boundary and transgranular locations. A low density of fine spherical particles, presumably β' - Al_3Zr or $\text{Al}_3(\text{Zr},\text{Li})$, was also observed within the grains. Weak streaks along [100] directions in the diffraction pattern suggested the presence of GP zones. Additionally, ~100 nm long needle-like precipitates of T_1 or Al_2CuLi phase were observed at scattered locations.

(5) The transverse tensile strengths for both the 214- and 430-RPM FSW specimens are inferior to those of the parent Al 2195 metal. The failure strains for the 430-RPM FSW specimens were about 30% lower than those for the 214-RPM specimens.

(6) All-weld metal tensile strengths for both 214- and 430-RPM specimens are similar-but lower than the parent Al 2195 metal. The 214-RPM processed welds showed a ductility of over 25% in the weld nugget as well as in the adjacent zone, while the 430-RPM weld showed a distinctly lower ductility in the weld nugget region. The all-weld properties were nearly symmetrical on either side of the weld-nugget centerline.

(7) Stress corrosion cracking data indicate an increased SCC susceptibility for the weld materials compared to parent Al 2195 material, with a slightly larger reduction for the transverse (T) orientation compared to the longitudinal (L) orientation (13% vs. 9%, respectively). Comparison of the % elongation results between air and aqueous NaCl environment also shows susceptibility to SCC for each of the materials, but to slightly different degrees than that shown by the tensile strength data.

(8) Screening data indicate that the fatigue crack growth rates in the HAZ and weld nugget regions are slightly lower than the rate for the base metal.

RECOMMENDATION FOR FUTURE WORK

- (1) Crystallographic orientation prediction at various locations relative to the tool path & comparison with EBSD results on FSW material.
- (2) Effect of post-weld isothermal aging treatments on the FSW microstructures, in particular, on precipitate growth at the sub-grain and grain boundaries.
- (3) Weld nugget & all-weld tensile properties in as-FSW vs. post-FSW-aged conditions.

(4) Corrosion behavior in as-FSW vs. post-FSW-aged conditions.

ACKNOWLEDGMENTS

This work was sponsored (in part) by the Air Force Office of Scientific Research, UASF, under grant/contract number F49620-01-1-0300 (Dr. Craig S. Hartley, Program Manager, Metallic Materials, AFOSR/NA). The views and conclusions contained herein are those of the authors and should not be interpreted as necessarily representing the official policies or endorsement, either expressed or implied, of the Air Force Office of Scientific Research or the U.S. Government. The author would like to acknowledge helpful comments and suggestions from Drs. Michael Henry, Ann Ritter, Christine Furstoss of GE Global Research, Dr. Kumar Jata of the Air Force Materials Laboratory, and Dr. William Arbegast of South Dakota School of Mines.

REFERENCES

1. W. M. Thomas, E. D. Nicholas, J. C. Needham, M. G. Murch, P. Templesmith, and C. J. Dawes, Friction Stir Butt Welding. International Patent Application No. PCT/GB92/02203 and GB Patent Appl. No. 9125978.8, Dec. 1991; U.S. Patent No. 5,460,317, Oct. 1995.
2. P. Threadgill, Friction Stir Welds in Aluminum Alloys - Preliminary Microstructural Assessment, *TWI Bulletin*, 38(2), 30-33 (1997).
3. W. J. Arbegast and P. J. Hartley, "Friction Stir Weld Technology Development at Lockheed Martin Michoud Space System – An Overview," *5th International Conference on Trends in Welding Research*, ASM International, Materials Park, OH, 541-546 (1999).
4. C. J. Dawes and W. M. Thomas. *TWI Bulletin*, 6, 124–127 (1995).
5. C. J. Dawes and W. M. Thomas. *Welding Journal*, 75(3), 41–46 (1996)
6. W. Thomas, C. Dawes, M. Gittos, and D. Andrews. *TWI Bulletin*, 3, 44–50 (1998).
7. J.-Q. Su, T. W. Nelson, R. Mishra, M. Mahoney. *Acta Materialia*, 51, 713-729 (2003).
8. M. W. Mahoney, C. G. Rhodes, J. G. Flintoff, R. A. Spurling, and W. H. Bingel. *Metall. Trans. A*, 29A, 1955–1964 (1998).
9. L. E. Murr, G. Liu, and J. C. McClure. *J. Mater. Sci. Lett.*, 16, 1801–1803 (1997).
10. O. V. Flores, C. Kennedy, L. E. Murr, D. Brown, S. Pappu, B. M. Nowak, and J. C. McClure. *Scripta Mater.*, 38(5), 703–708 (1998).

11. T. W. Nelson, B. Hunsaker, and D. P. Field. in *Proceedings of 1st International Symposium on Friction Stir Welding*, Thousand Oaks, CA, USA, 14–16 June 1999.
12. G. Liu, L. E. Murr, C. S. Niou, J. C. McClure, and F. R. Vega. *Scripta Mater.*, 37(3), 355–361 (1997).
13. L. E. Murr, G. Liu, and J. C. McClure. *J. Mater. Sci.*, 33, 1243–1251 (1998).
14. T. J. Lienert and R. J. Grylls, in *Proceedings of 1st International Symposium on Friction Stir Welding*, Thousand Oaks, CA, USA, 14–16 June 1999.
15. C. G. Rhodes, M. W. Mahoney, W. H. Bingel, R. A. Spurling, and C. C. Bampton. *Scripta Mater.*, 36(1), 69–75 (1997).
16. M. Strangwood, J. E. Berry, D. P. Cleugh, A. J. Leonard, and P. L. Threadgill, in *Proceedings of 1st International Symposium on Friction Stir Welding*, Thousand Oaks, CA, USA, 14–16 June 1999.
17. G. Biallas, R. Braun, C. D. Donne, G. Staniek, and W. A. Kaysser , in *Proceedings of 1st International Symposium on Friction Stir Welding*, Thousand Oaks, CA, USA, 14–16 June 1999.
18. L.-E. Svensson and L. Karlsson, in *Proceedings of 1st International Symposium on Friction Stir Welding*, Thousand Oaks, CA, USA, 14–16 June 1999.
19. Ø. Frigaard, Ø. Grong, J. Hjelen, S. Gulbrandsen- Dahl, and O.T.Midling, in *Proceedings of 1st International Symposium on Friction Stir Welding*, Thousand Oaks, CA, USA, 14–16 June 1999.
20. K. V. Jata, K. K. Sankaran and J. J. Ruschau, *Metallurgical and Materials Transactions*, 31 A, 2181-2192 (2000).
21. Z. X. Li, W. J. Arbegast, P. J. Hartley, and E. I. Meletis, “Microstructure Characterization and Stress Corrosion Evaluation of Friction Stir Welded Al 2195 and Al 2219 Alloys,” *Proc. 5th Intl. Conf. on Trends in Welding Research*, ASM International, Materials Park, OH, 568-573 (1999).
22. G. Oertelt, S. S. Babu, S. A. David, and E. A. Kenik, Effect of Thermal Cycling on Friction Stir Welds of 2195 Aluminum Alloy, *Welding Research Supplement*, March, 71s-79s (2001).
23. G. Bussu and P. E. Irving, in *Proceedings of 1st International Symposium on Friction Stir Welding*, Thousand Oaks, CA, USA, 14–16 June 1999.
24. W. Hu and E. I. Meletis, *Mater. Sci. Forum*, 331-337, 1683-1688 (2000).
25. J. Corral, E. A. Trillo, Y. Li, and L. E. Murr, *J. Mater. Sci. Lett.*, 19, 2117-2122 (2000).

26. J. Lumsden III, M. Mahoney, G. Pollock, D. Waldron, and A. Guinasso, in *Proceedings of 1st International Symposium on Friction Stir Welding*, Thousand Oaks, CA, USA, 14–16 June 1999.
27. Z. Feng, J.E. Gould, and T.J. Lienert. In *Proceedings of Hot Deformation of Aluminum Alloys II*. Eds. L.A. Lalli, T.R. Bieler and S.R. MacEwen. The Minerals, Metals & Materials Society (1998).
28. J.C. McClure, T. Tang, L.E. Murr, X. Guo, Z. Feng, and J.E. Gould, in *5th International Conference on Trends in Welding Research*, ASM International, Materials Park, OH, 590-598 (1999).
29. M. J. Russell and H. R. Shercliff, in *Proceedings of 1st International Symposium on Friction Stir Welding*, Thousand Oaks, CA, USA, 14–16 June 1999.
30. Y. J. Chao and X. Qi, in *Proceedings of 1st International Symposium on Friction Stir Welding*, Thousand Oaks, CA, USA, 14–16 June 1999
31. O. Frigaard, O. Grong, B. Bjorneklett, and O. T. Midling, in *Proceedings of 1st International Symposium on Friction Stir Welding*, Thousand Oaks, CA, USA, 14–16 June 1999.
32. P. Reynolds. University of South Carolina, Columbia, SC. Private communication (1998).
33. P.C. Sweeney, and J.F. Rhodes. Int'l Gas Turb. Conf & Expo, June 7–10, 1999, Indianapolis, IN, Paper No. 99-GT-142.
34. J.J. Stiglich, C.C. Bishop, J.A. Daleo, D.H. Boone, T.E. Eelkema, in *Proceedings of the ASM Gas Turbines Materials Tech. Conf.*, Rosemont, IL, 12–15 Oct. 1998.
35. N. Nirmalan. Measurement of Internal Heat Transfer Using Transient IR Technique, GE, Schenectady, New York; private communication (1999).
36. S. A. Sargent, C. R. Hedlund, P. M. Ligrani, *Meas. Sci. and Tech.*, 9, 1974–1981 (1998).
37. C.R. Hedlund. Heat Transfer and Flow Behavior in a Swirl Chamber with Helical Flow, Ph.D. dissertation, Univ. of Utah (1998).
38. C.R. Hedlund, P.M. Ligrani, H.-K. Moon, B. Glezer, *ASME J. Turbomachinery*, 121, 804–813 (1999).
39. T. U. Seidel and A. P. Reynolds, *Metall. Mater. Trans. A*, 32A, 2879–2884 (2001).
40. K. V. Jata and S. L. Semiatin, *Scripta Mater.*, 43, 743–749 (2000).
41. W. J. Arbegast, K. S. Baker, and P. J. Hartley, in *Proc. 5th Intl. Conf. on Trends in*

Welding Research, ASM International, Materials Park, OH, 558-562 (1999).

42. N.J.H. Holroyd and G.M. Scamans, "Slow-Strain-Rate Stress Corrosion Testing of Aluminum Alloys", Environment-Sensitive Fracture: Evaluation and Comparison of Test Methods, ASTM STP 821, S.W. Dean, E.N. Pugh, and G.M. Ugiansky, eds., American Society for Testing and Materials, Philadelphia, 202-241 (1984).
43. Corrosion of Aluminum and Aluminum Alloys, E.H. Hollingsworth and H.Y. Hunsicker, ASM Handbook Vol. 13 Corrosion, J.R. Davis et al, eds., ASM International, Materials Park, OH, 583-609 (1987).
44. Reji John and K.V. Jata, "Residual Stress Effects on Near-Threshold Fatigue Crack Growth in Friction Stir Welds, TMS 2001, Indianapolis, IN.

Table 1. Summary of microstructures observed in friction stir welded aluminum alloys.

Alloy	Details	Reference
1100	Equiaxed dynamically recrystallized grains with large misorientations; recrystallized grain size correlates with dislocation substructure size in base metal. No contribution from prior deformation to dynamic recrystallization. Precipitates (Al_xFe -type) from parent metal fragmented/deformed during FSW and distributed homogeneously within FSW zone. Weld-zone microstructure developed varying crystallographic textures depending on position in weld.	(9, 10, 11)
2xxx	2014: Breakup and dissolution of intermetallic particles in weld nugget. Over-aging of precipitates in HAZ. 2024: Fracture of primary particles. Aging of hardening particles in HAZ. 2195: Equiaxed DRZ; No T1 (Al_2CuLi); Grains with different recovery. Observed GP zones, T_B ($\text{Al}_7\text{Cu}_4\text{Li}$), Al_3Zr	(16, 17, 21, 22)
6xxx	6061: Range of precipitation microstructures observed suggest a strong dependence of local temperature and strain gradient within the weld. Microstructures representative of continuous and discontinuous, as well as localized precipitation. Homogeneous precipitates (Al_xMgSi -type) in FSW zone, lath-type Widmanstatten precipitates (Al_xMgSiCu -type) in transition zone, coherent GP-type ppts. near weld-zone bottom. Absence of precipitates in the top stir zone (highest temperature, strain, and strain gradients) indicative of local temperatures exceeding precipitate solvus temperatures. 6082: Hardening ppts. (Mg_5Si_6) dissolved in both weld nugget and HAZ. Coarse $\text{AlFe}(\text{Mn})\text{Si}$ or Mg_2Si particles and fine Al-Mn-Si dispersoids in weld nugget. Needlelike $\text{Mg}_{1.7}\text{Si}$ precipitates nucleated on dispersoids in HAZ adjacent to weld. No evidence of GP zones in weld nugget or HAZ.	(12, 13, 14, 18, 19)
7xxx	7075: Dissolution of all precipitates, and reprecipitation of strengthening ppt ($\text{Mg}_{32}(\text{Al},\text{Zn})_{49}$ or $\text{MgZn}_2(\text{AlCu})$) as randomly oriented intragranular plates; evidence of temperature excursion above solvus temperatures. Fine recrystallized, equiaxed grain structure in weld nugget. Evidence of mechanical fracture of precipitates. Over-aging of precipitates in HAZ region. 7108: Microstructure in plastically deformed regions showed dynamic recovery effects, with existence of both low-angle and high-angle grain boundaries. Indirect evidence of local melting and formation of liquid film at tool/matrix interface. 7050: Fine equiaxed grains in weld nugget; some grains had high dislocation density, with dislocations pinned by Al_3Zr dispersoids and $\text{Al}_7\text{Cu}_2\text{Fe}$ inclusions. Evidence of particle breakup due to FSW. Dissolution of strengthening precipitates in weld nugget. Coarsening of strengthening phases and formation of precipitate-free zones (PFZs) in HAZ. Post-weld heat treatment resulted in formation of GP zones in weld nugget.	(8, 15, 16, 19, 20)

LIST OF FIGURES

Figure 1. Schematic description of the friction stir welding process.

Figure 2: (a) FSW run in progress on an instrumented Al 6061 plate; (b) FSW run on the Al 2195 plate.

Figure 3. Initial bead-on-plate FSW runs on Al 6061 plates.

Figure 4. Temperature profiles generated in the Al 6061 plate during the FSW tool plunge as well as during tool traversal: (a) at the underside of the plate along the joint line: (b) along the joint line.

Figures 5 (a) and (b): Temperature profiles obtained from the top of the Al 6061 plate at locations 25 mm (1") to the left as well as right of the joint line; (c) Location of thermocouples relative to tool movement and weld joint.

Figure 6. Still thermal image captured during FSW of Al 2195.

Figure 7. Temperature profiles taken at selected locations away from the FSW tool as shown in Fig.6: (a) Axial temperature profile along the weld joint; (b) Lateral temperature profile normal to the weld joint.

Figure 8. Temperature profiles as a function of time at the top of the workpiece in-line with the traversing tool for 2 different tool rotation speeds (214 and 430 RPM). Thermocouples were located at points 50 mm (2"), 100 mm (4"), 150 mm (6"), and 200 mm (8") from the start of the weld.

Figure 9. Temperature profiles as a function of time at the bottom of the workpiece in-line with the traversing tool for 2 different tool rotation speeds (214 and 430 RPM). Thermocouples were located under the plunge location and at distances of 50 mm (2"), 100 mm (4"), 150 mm (6"), and 200 mm (8") from the start of the weld.

Figures 10 (a) and (b): Temperature profiles obtained from the top of the Al 2195 plate at locations 25 mm (1") to the left (LE) as well as right (TE) of the joint line – the thermocouples are positioned 50 mm (2") apart from each other along both TE and LE; (c) Location of thermocouples relative to tool movement and weld joint.

Figure 11. Secondary electron SEM microstructures of FSW Al 2195 for two different tool rotation speeds (214 and 430 RPM).

Figure 12. SEM microstructures of various zones within the FSW region in the 214-RPM processed Al 2195.

Figure 13. SEM microstructures of various zones within the FSW region in the 430-RPM processed Al 2195.

Figure 14. SEM microstructures of FSW Al 2195 for 214 RPM tool rotation speed: (a) Dynamically recrystallized zone (DXZ) from the center of the weld nugget; (b) transition region between the DXZ region, thermomechanically affected zone (TMZ), and the heat-affected zone (HAZ).

Figure 15. SEM microstructures of FSW Al 2195 for two different tool rotation speeds (214 and 430 RPM): (a) and (b) – from the center of the weld nugget; (c) and (d) - from the dynamically recrystallized zone (DXZ) close to the thermomechanically affected zone (TMZ).

Figure 16. Measured temperatures during FSW of Al 2195 vs. predicted phase equilibria (from [22]) in Al 2195.

Figure 17. TEM images of precipitates observed in the DXZ region: (a): Intergranular $\text{Al}_7\text{Cu}_4\text{Li}$ or T_B precipitates; (b) Transgranular $\text{Al}_7\text{Cu}_4\text{Li}$ precipitates; (c) $\text{Ll}_2 \beta'$ - Al_3Zr or $\text{Al}_3(\text{Zr},\text{Li})$ particles; (d) needle-like precipitates (may be T_1 or Al_2CuLi).

Figure 18. Euler map of left side of weld and base metal.

Figure 19. Top: Expanded Euler map of base metal region (shown in Fig. 18); Bottom: Pole figures of base metal region (equivalent to as received rolled plate). Pole figure peak is 11.78.

Figure 20. Top: Expanded Euler map of transition region (shown in Fig. 18) from base metal to TMZ/HAZ regions where the grains are rotated by their proximity to the stir zone; Bottom: Pole figures of this transition region.

Figure 21. Top: Expanded Euler map of weld nugget DXZ region (shown in Fig. 18); Bottom: Pole figures of weld nugget region.

Figure 22. Configurations of transverse and longitudinal tensile specimens relative to the FSW joint.

Figure 23. Transverse tensile data for 214- and 430-RPM FSW specimens, compared with data for parent AA 2195 metal from Li et al. [21] and FSW Al 2195 from Arbegast et al. [41]: (a) Tensile strength; (b) % Elongation.

Figure 24. Failure location relative to the FS joint in the transverse tensile-tested specimens (a) 214-RPM and (b) 430-RPM FSW.

Figure 25. Longitudinal (al-weld metal) tensile data for 214- and 430-RPM FSW specimens, compared with data for parent AA 2195 metal from Li et al. [21]: (a) Tensile strength; (b) % Elongation.

Figure 26. SCC data for 214-RPM FSW specimens compared with results for air and parent Al 2195 material (a) Tensile strength; (b) % Elongation.

Figure 27. Specimen orientations for fatigue crack testing.

Figure 28. Fatigue crack growth rates (da/dN) vs. cyclic stress intensity (ΔK) in the HAZ and weld nugget regions compared with those in the base metal.

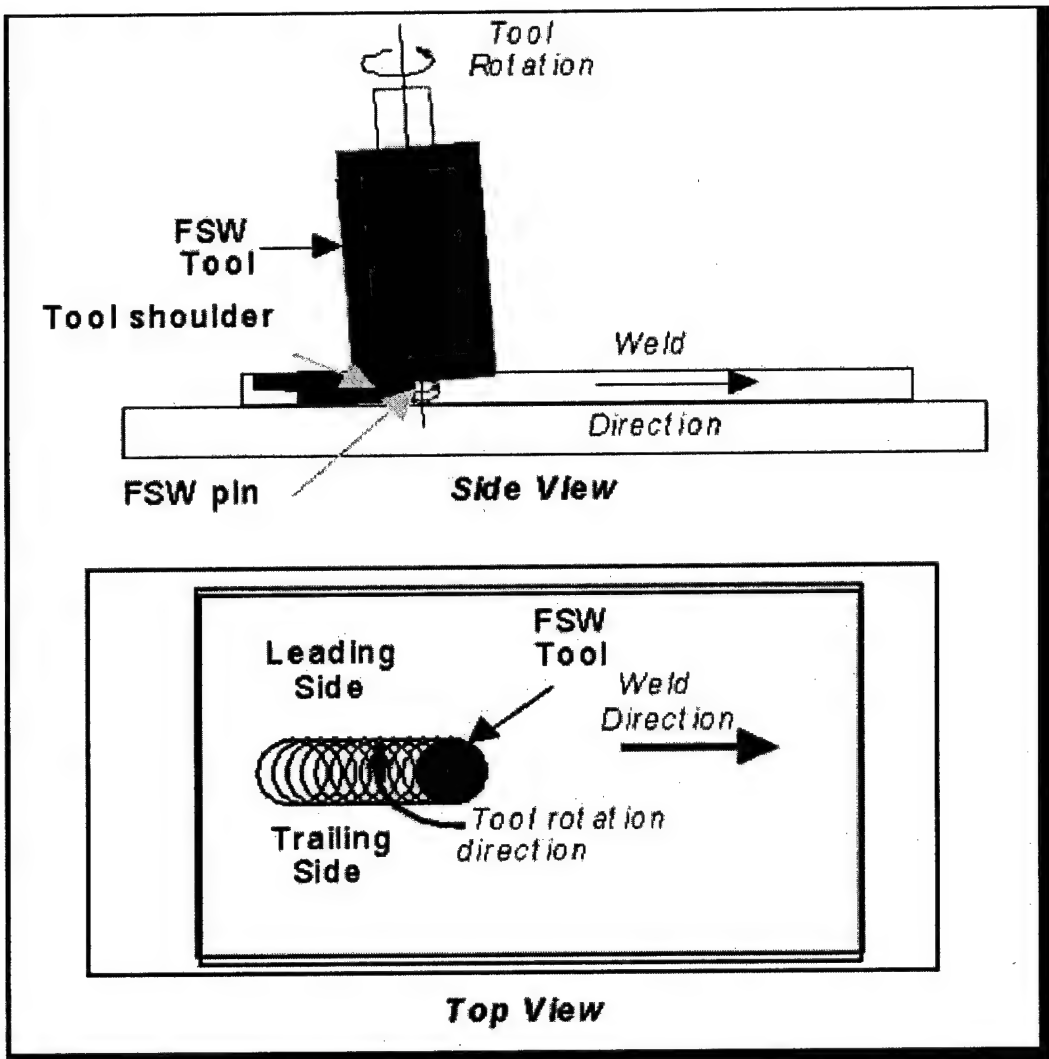


Figure 1. Schematic description of the friction stir welding process.

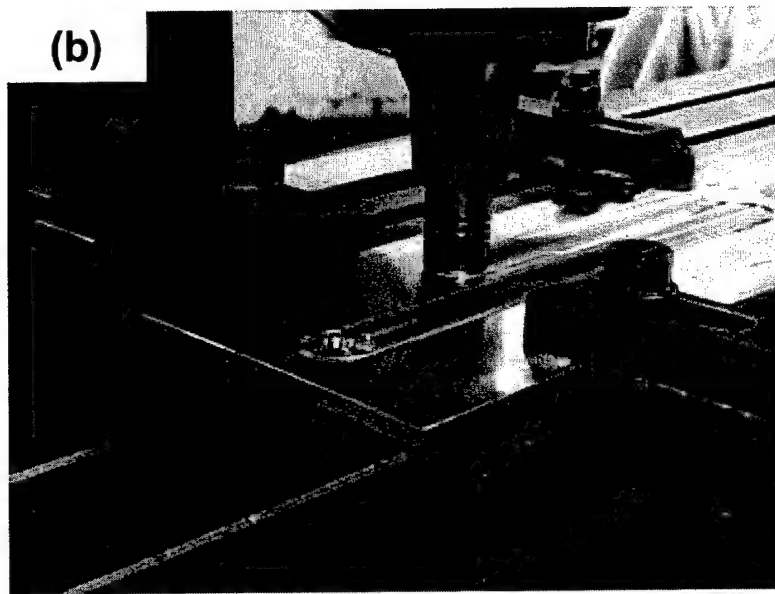
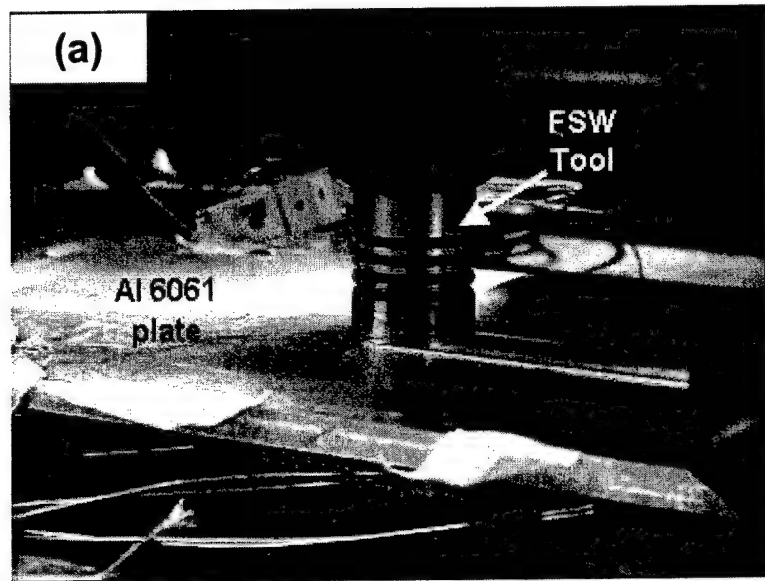


Figure 2: (a) FSW run in progress on an instrumented Al 6061 plate; (b) FSW run on the Al 2195 plate.

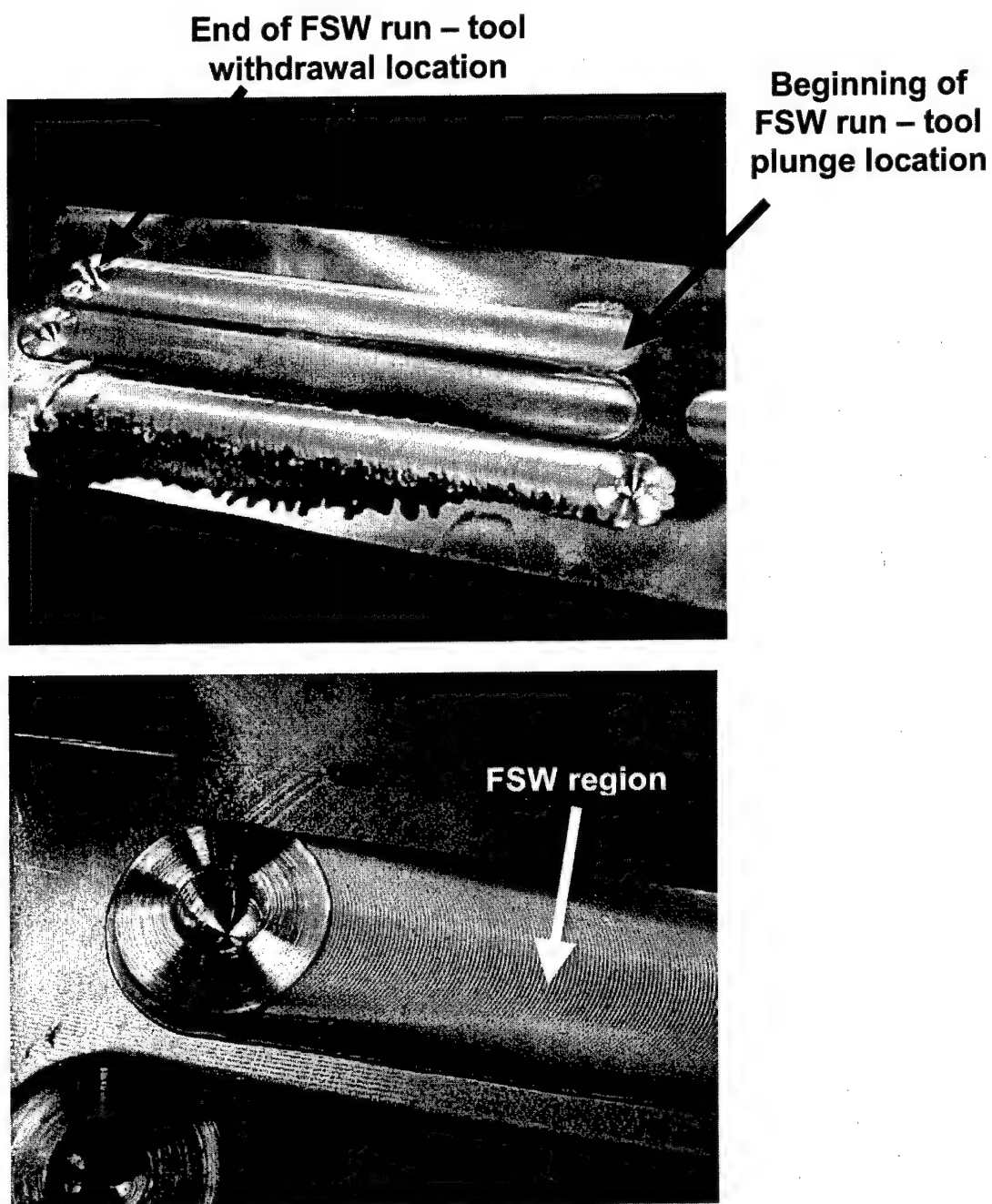
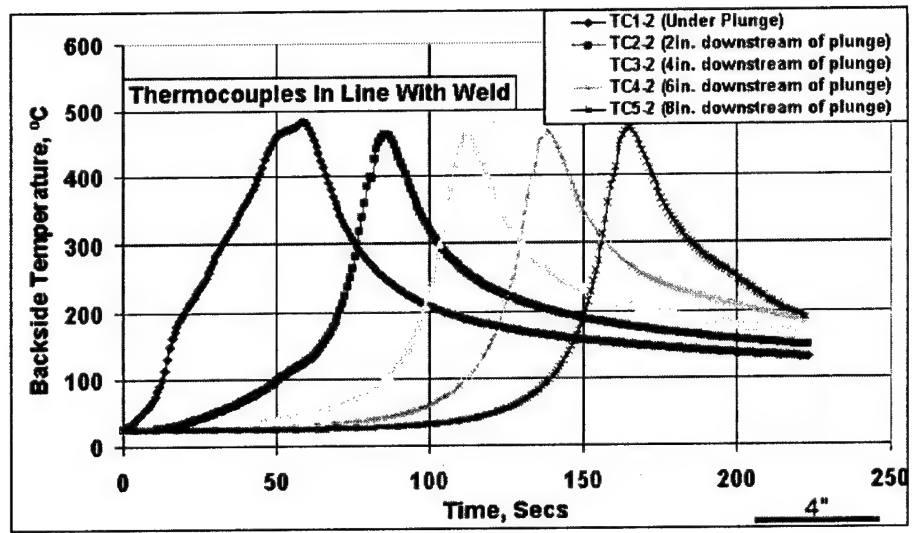
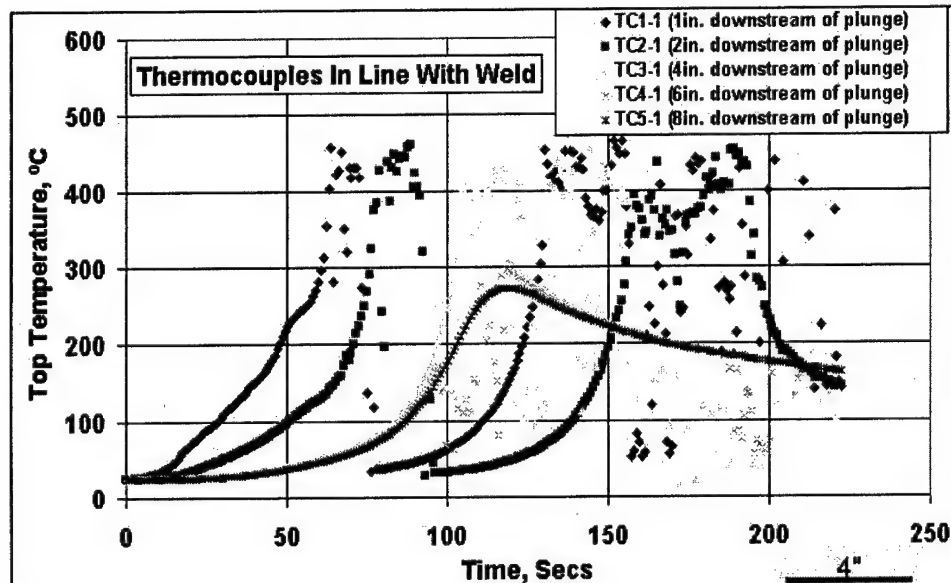


Figure 3. Initial bead-on-plate FSW runs on Al 6061 plates.

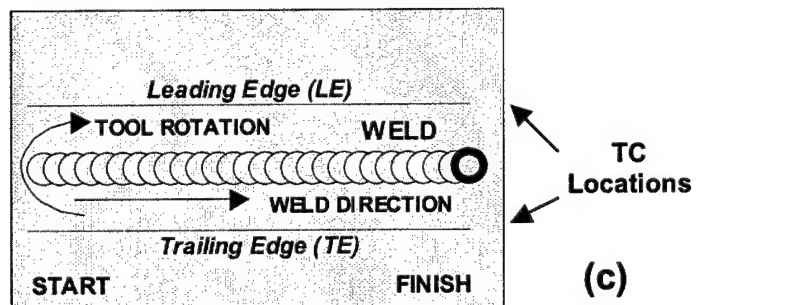
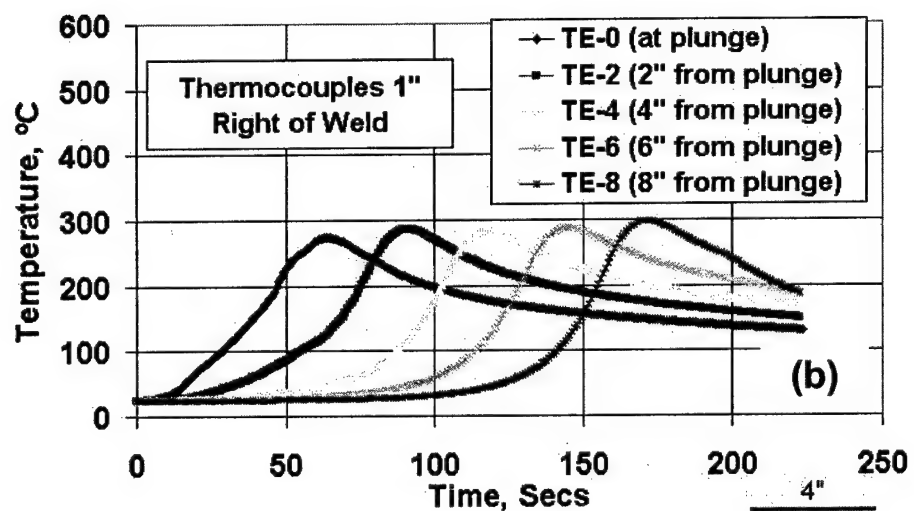
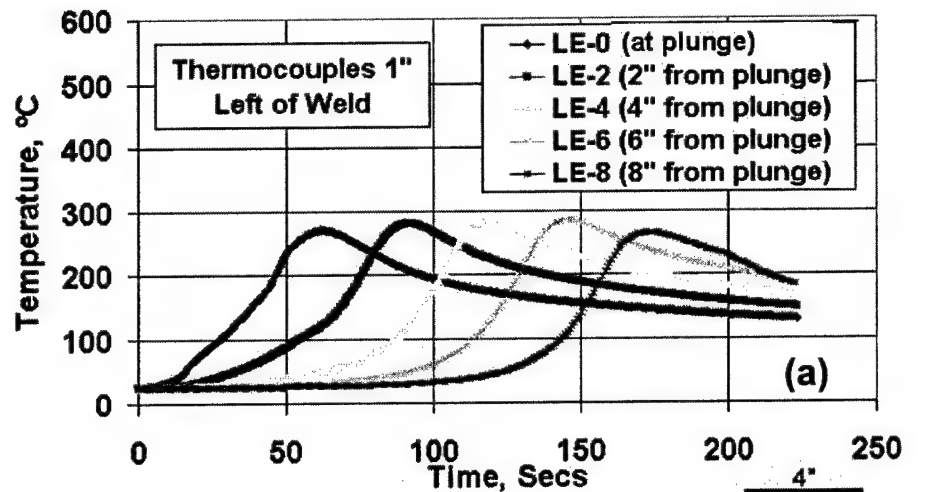


(a)



(b)

Figure 4. Temperature profiles generated in the Al 6061 plate during the FSW tool plunge as well as during tool traversal: (a) at the underside of the plate along the joint line; (b) along the joint line.



Figures 5 (a) and (b): Temperature profiles obtained from the top of the Al 6061 plate at locations 25 mm (1") to the left as well as right of the joint line; (c) Location of thermocouples relative to tool movement and weld joint.

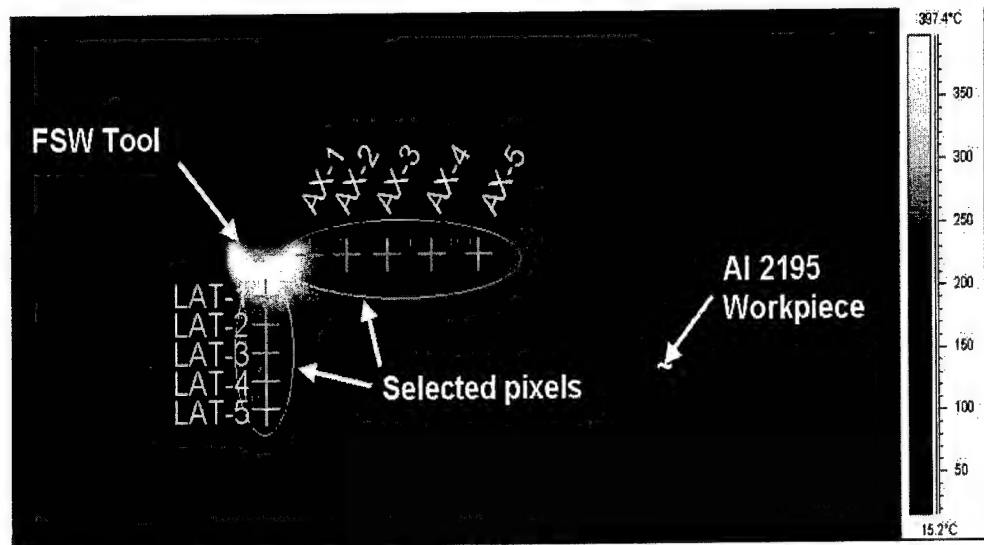


Figure 6. Still thermal image captured during FSW of Al 2195.

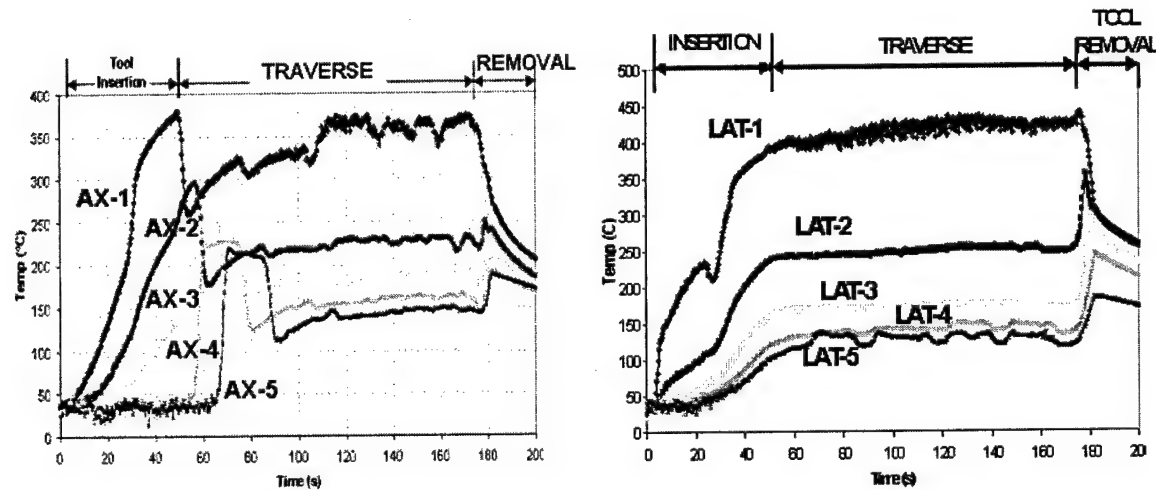


Figure 7. Temperature profiles taken at selected locations away from the FSW tool as shown in Fig.6: (a) Axial temperature profile along the weld joint; (b) Lateral temperature profile normal to the weld joint.

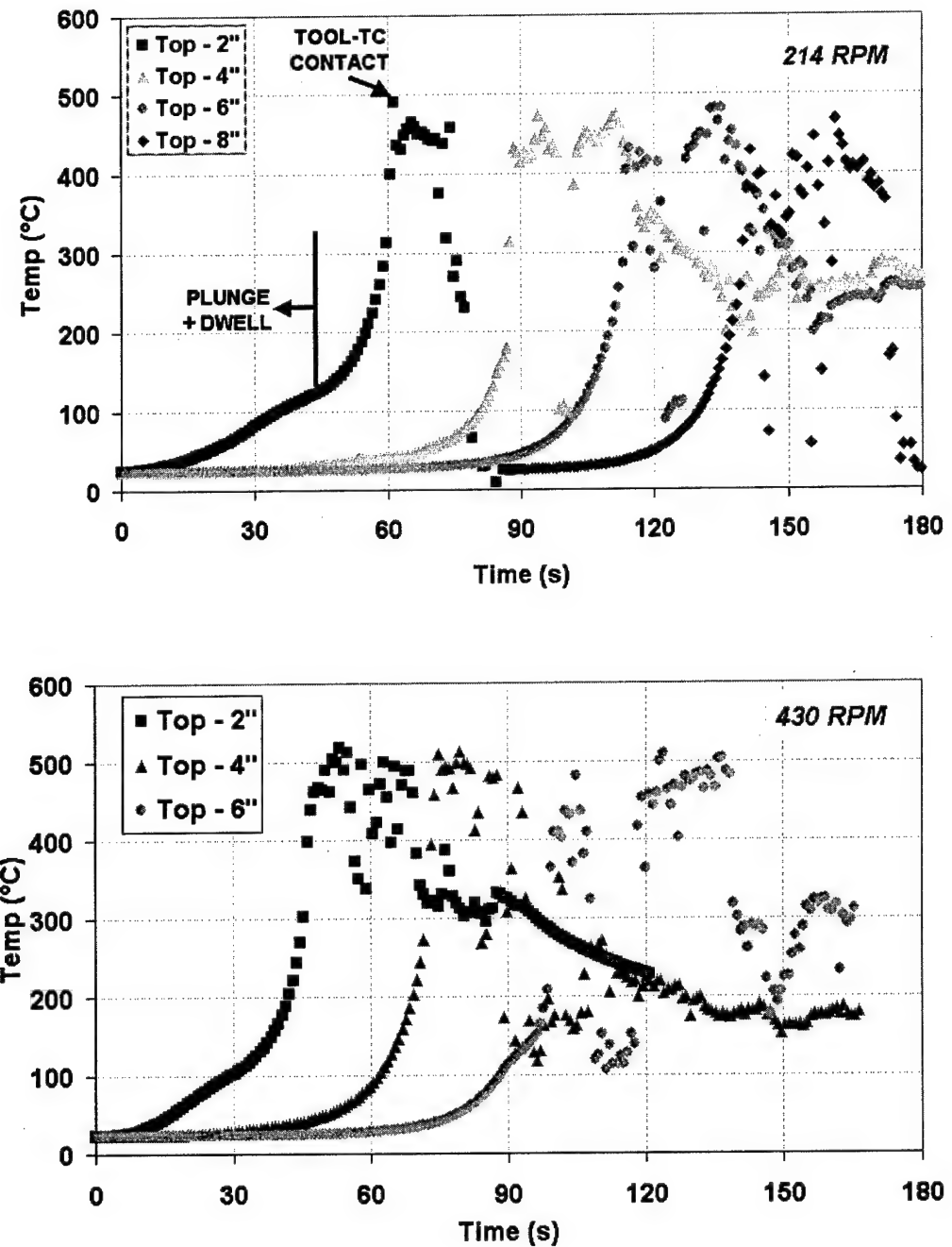


Figure 8. Temperature profiles as a function of time at the top of the workpiece in-line with the traversing tool for 2 different tool rotation speeds (214 and 430 RPM). Thermocouples were located at points 50 mm (2"), 100 mm (4"), 150 mm (6"), and 200 mm (8") from the start of the weld.

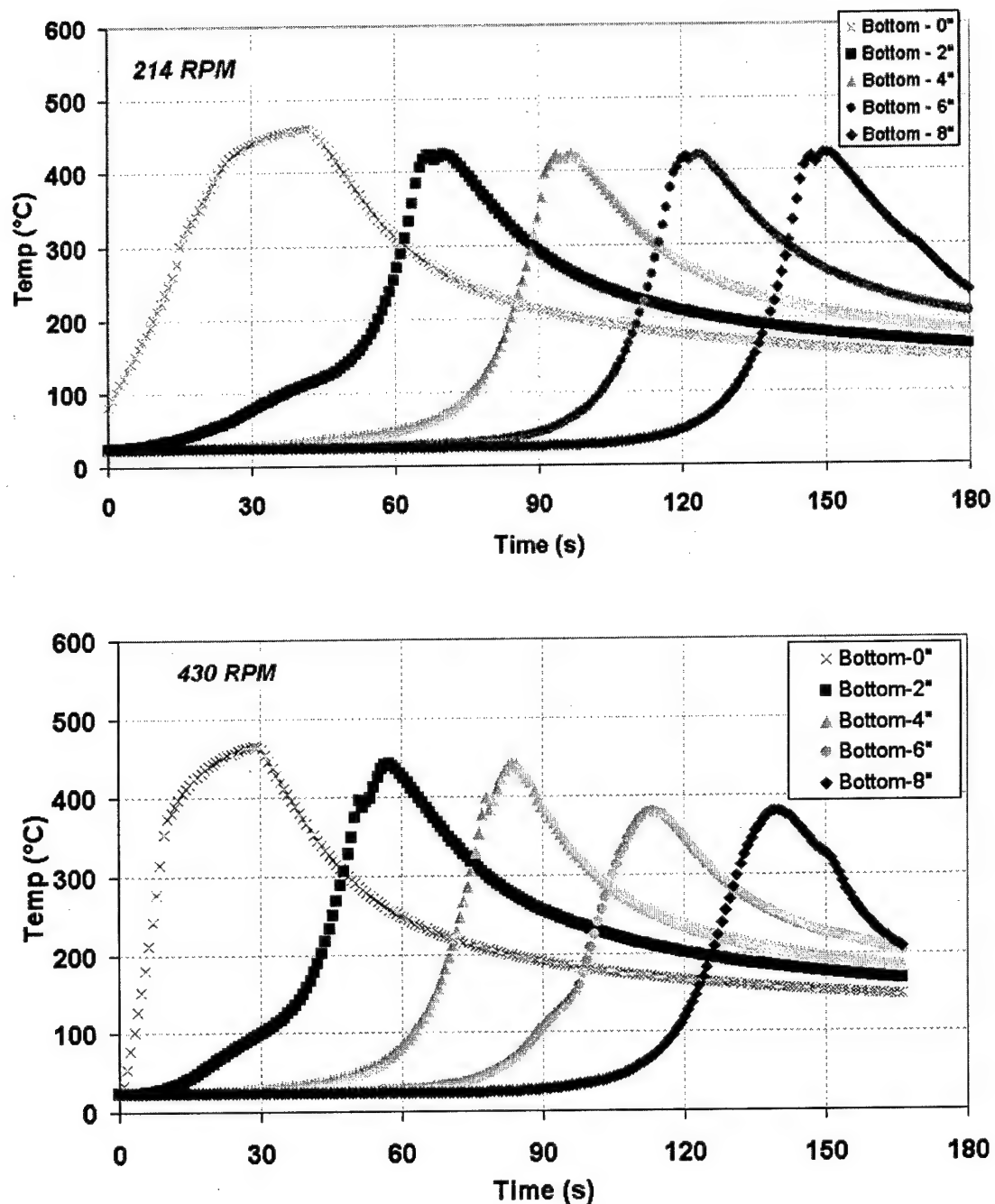
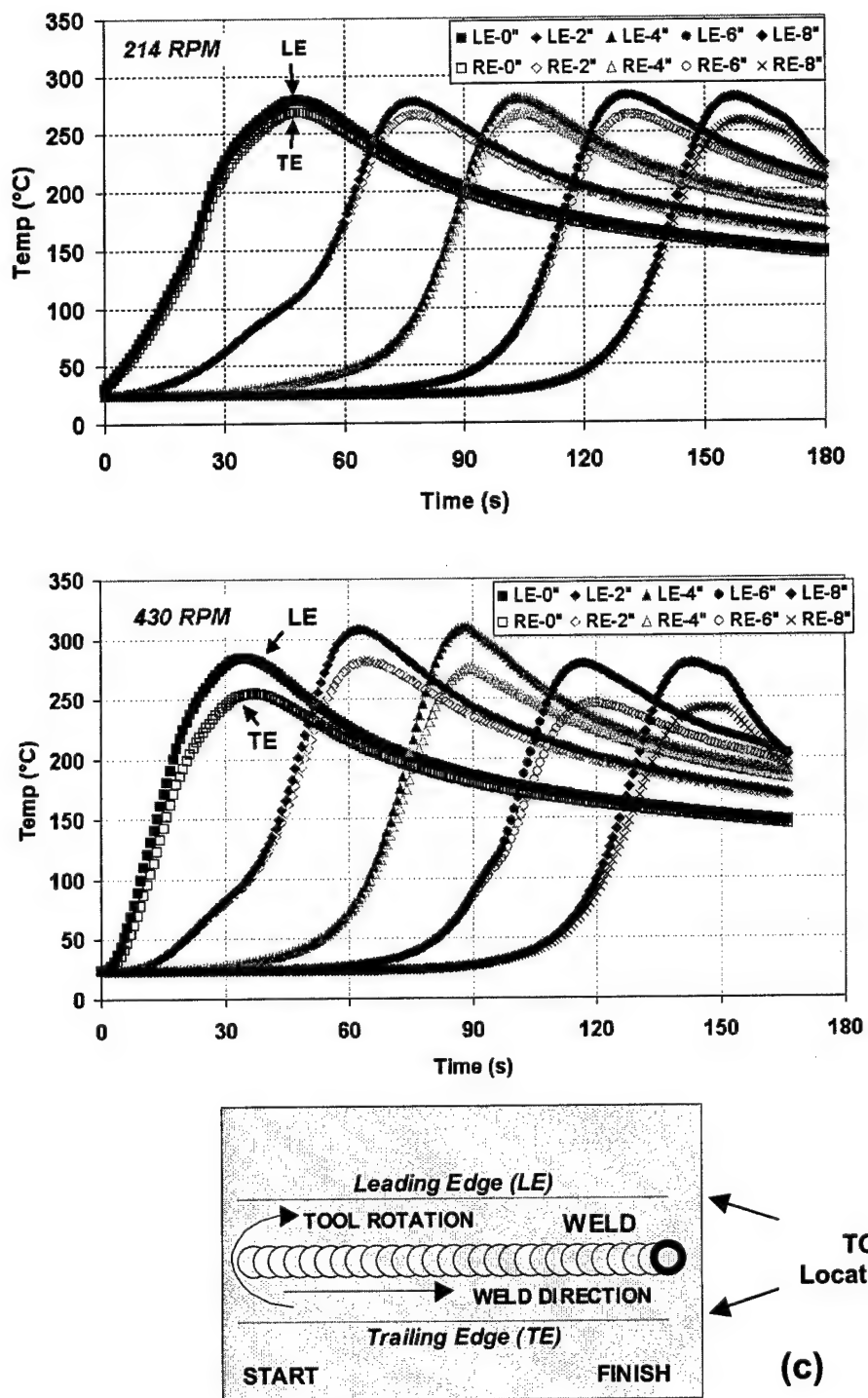


Figure 9. Temperature profiles as a function of time at the bottom of the workpiece in-line with the traversing tool for 2 different tool rotation speeds (214 and 430 RPM). Thermocouples were located under the plunge location and at distances of 50 mm (2"), 100 mm (4"), 150 mm (6"), and 200 mm (8") from the start of the weld.



Figures 10 (a) and (b): Temperature profiles obtained from the top of the Al 2195 plate at locations 25 mm (1") to the left (LE) as well as right (TE) of the joint line – the thermocouples are positioned 50 mm (2") apart from each other along both TE and LE; (c) Location of thermocouples relative to tool movement and weld joint.

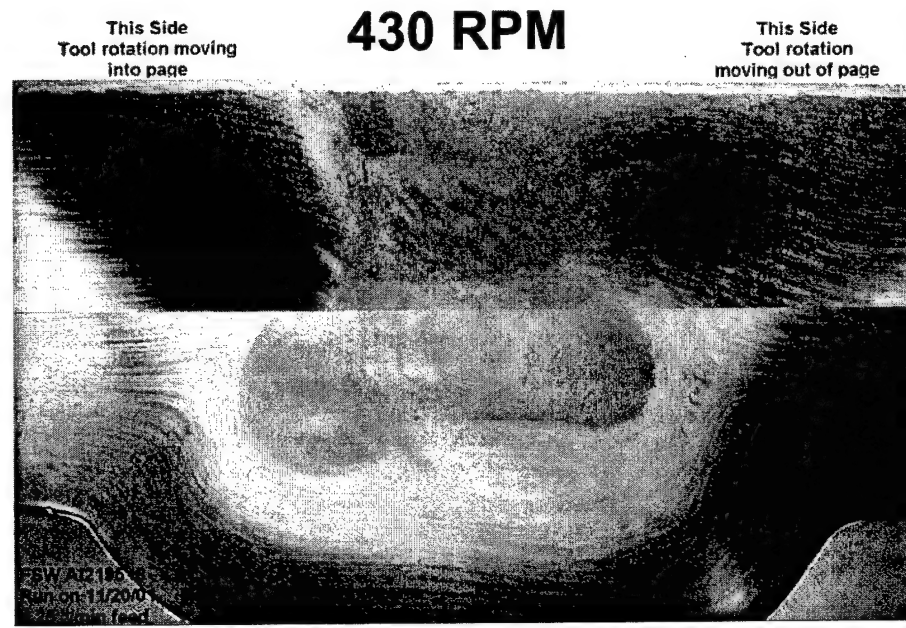
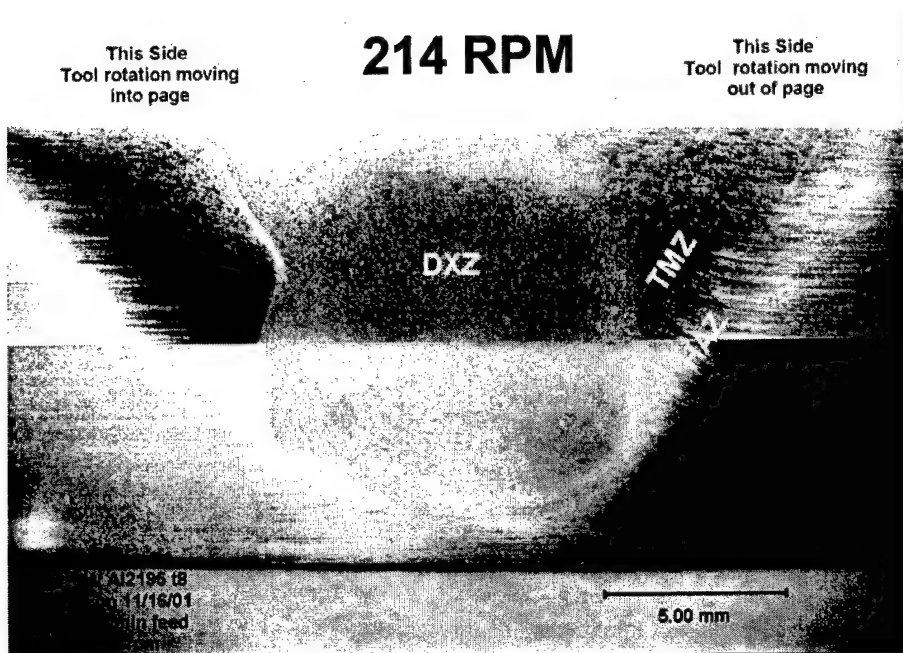


Figure 11. Secondary electron SEM microstructures of FSW Al 2195 for two different tool rotation speeds (214 and 430 RPM).

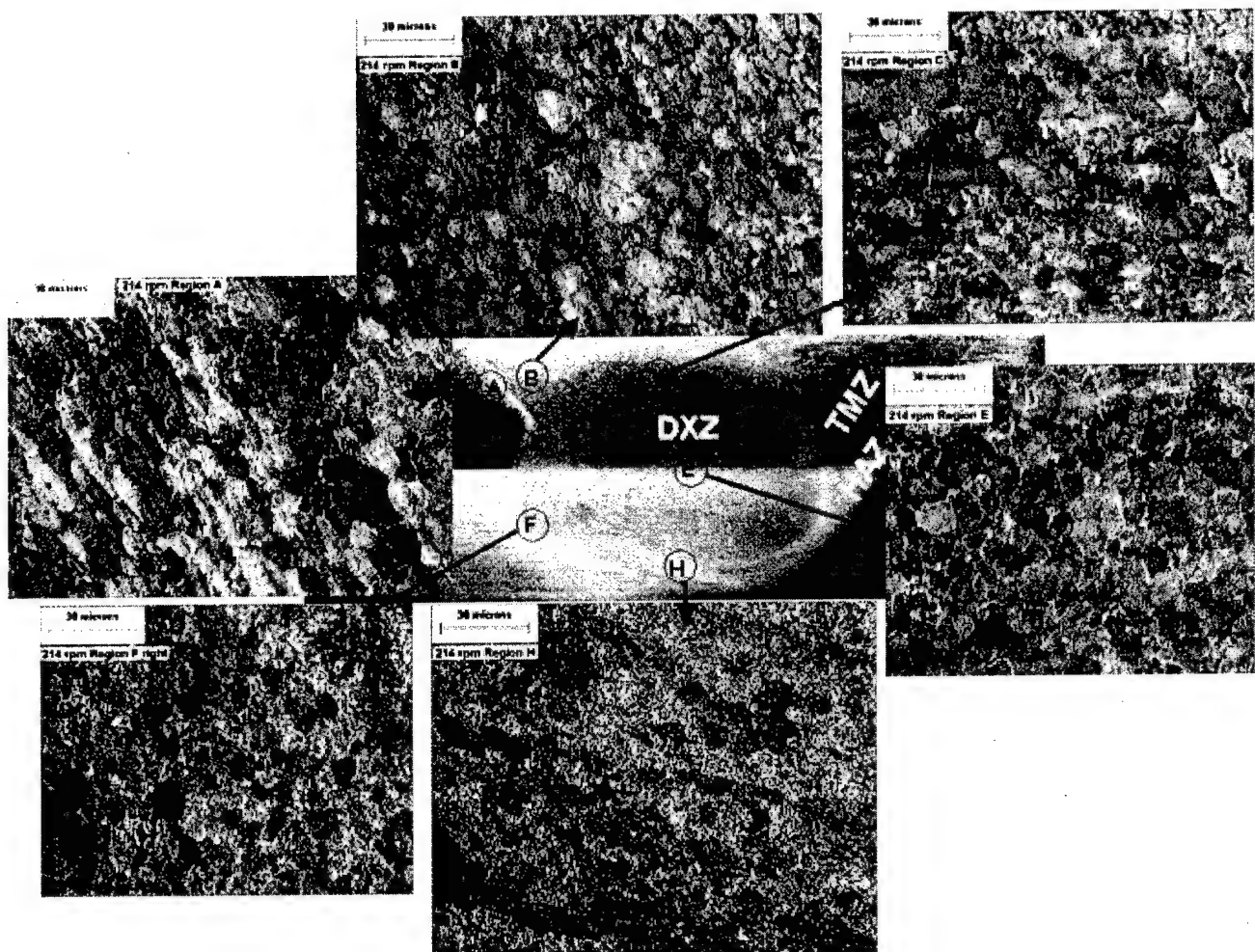


Figure 12. SEM microstructures of various zones within the FSW region in the 214-RPM processed Al 2195.

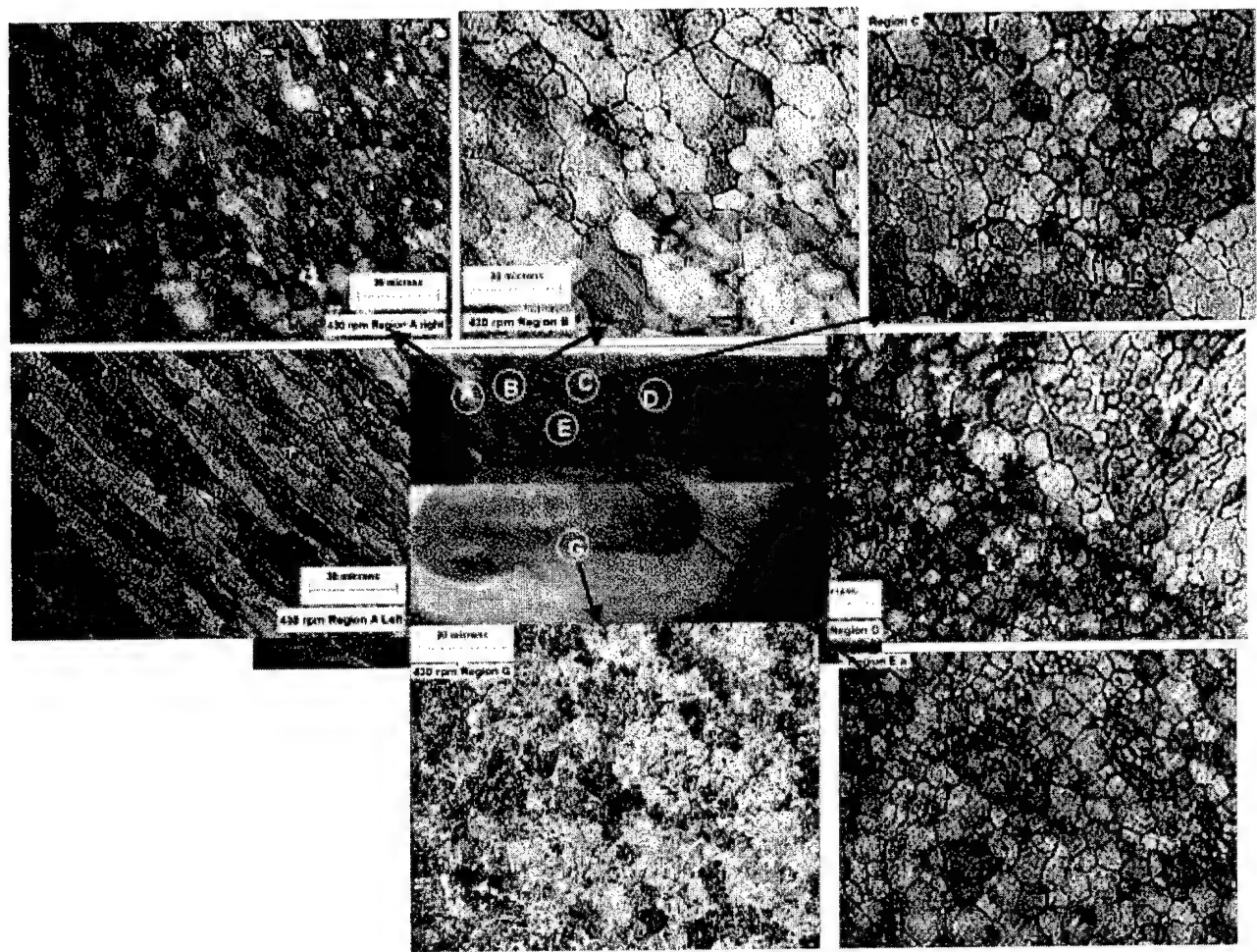


Figure 13. SEM microstructures of various zones within the FSW region in the 430-RPM processed Al 2195.

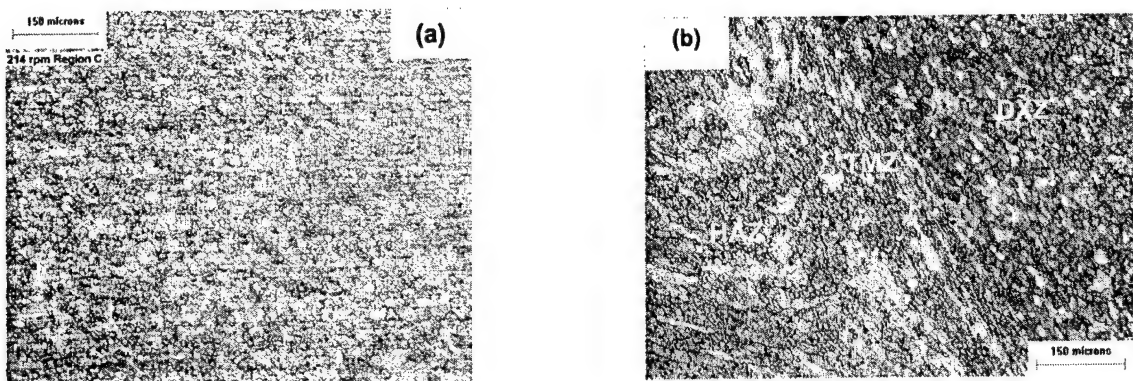


Figure 14. SEM microstructures of FSW Al 2195 for 214 RPM tool rotation speed: (a) Dynamically recrystallized zone (DXZ) from the center of the weld nugget; (b) transition region between the DXZ region, thermomechanically affected zone (TMZ), and the heat-affected zone (HAZ).

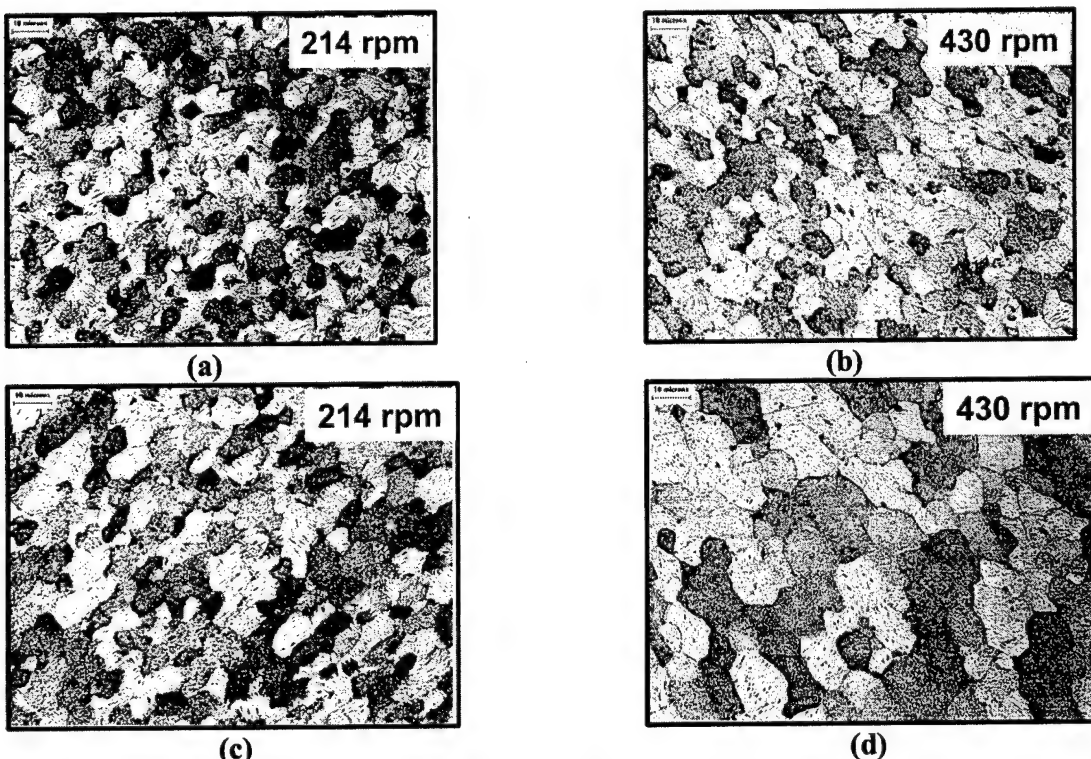


Figure 15. SEM microstructures of FSW AA2195 for two different tool rotation speeds (214 and 430 RPM): (a) and (b) – from the center of the weld nugget; (c) and (d) - from the dynamically recrystallized zone (DXZ) close to the thermomechanically affected zone (TMZ).

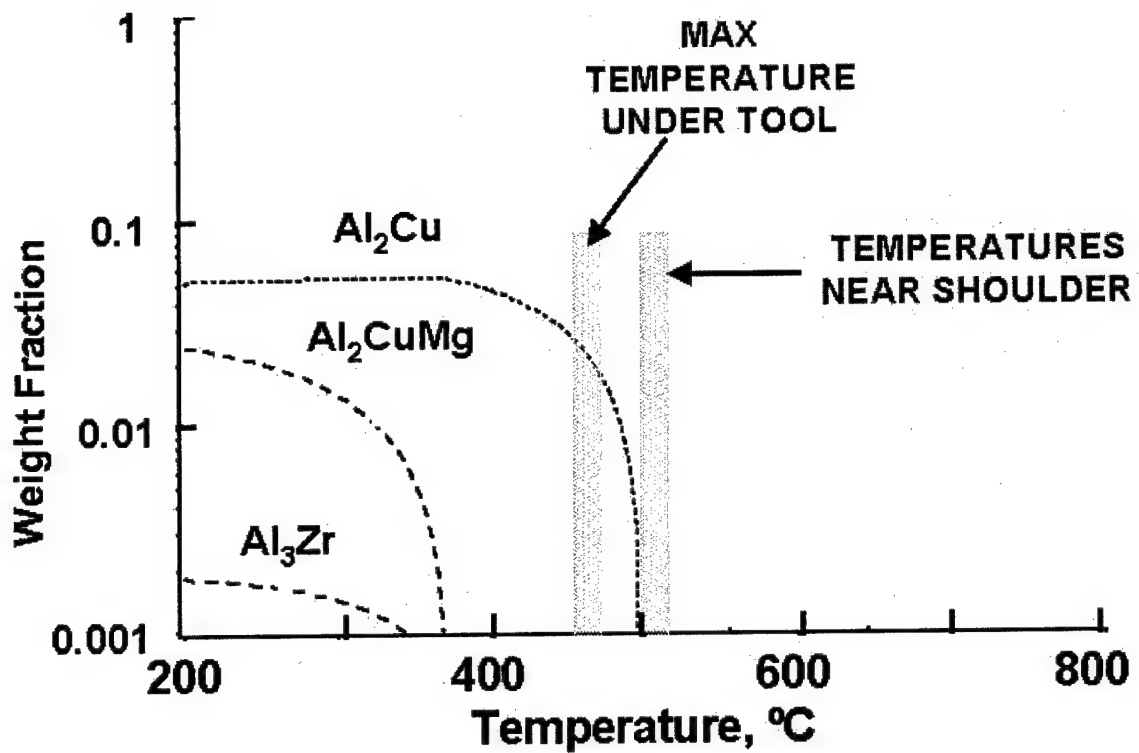
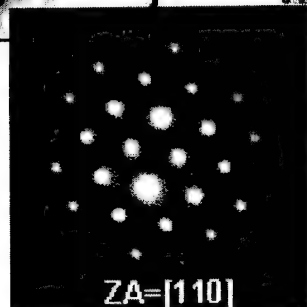
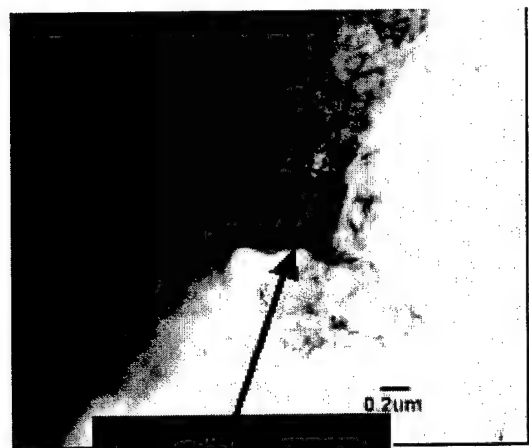
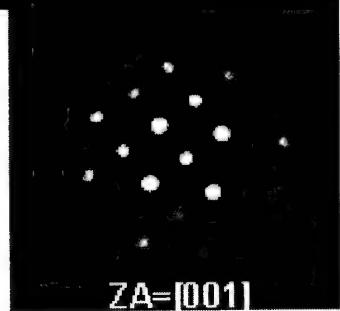
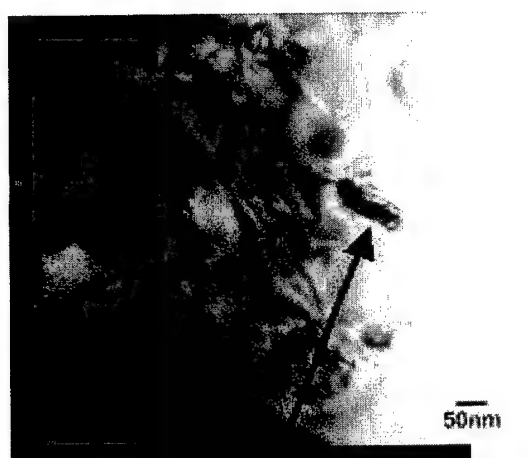


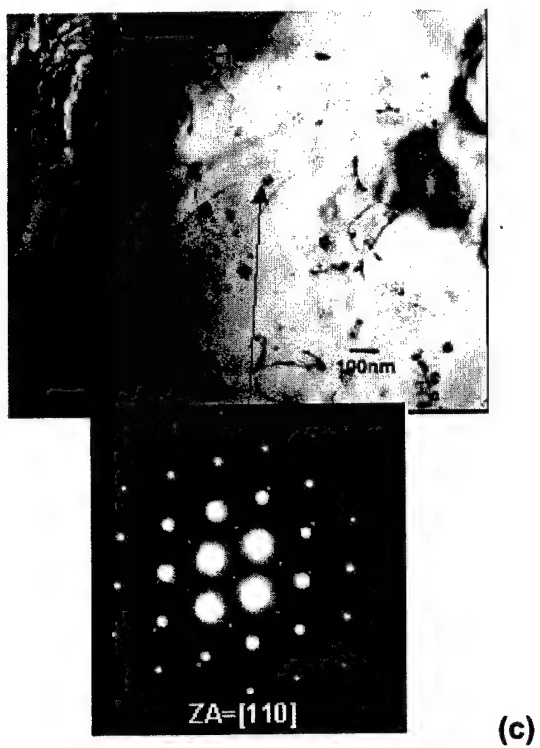
Figure 16: Measured temperatures during FSW of Al 2195 vs. predicted phase equilibria (from [22]) in Al 2195.



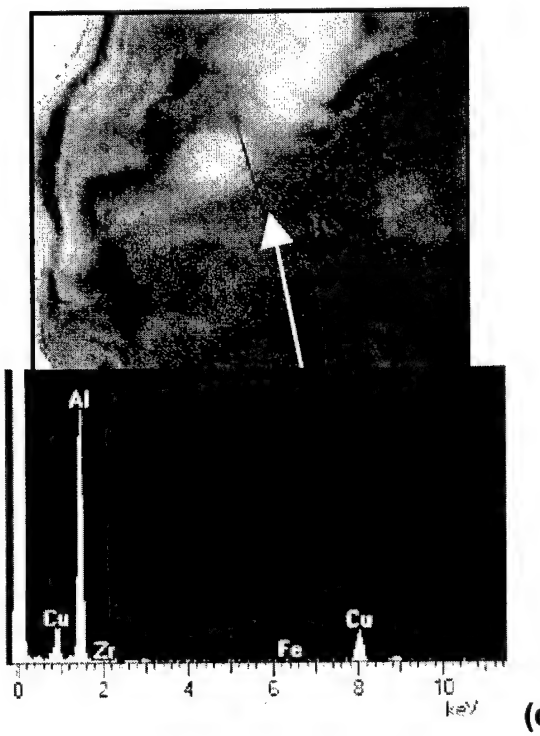
(a)



(b)



(c)



(d)

Figure 17. TEM images of precipitates observed in the DXZ region: (a): Intergranular $\text{Al}_7\text{Cu}_4\text{Li}$ or T_B precipitates; (b) Transgranular $\text{Al}_7\text{Cu}_4\text{Li}$ precipitates; (c) $L1_2$ β' - Al_3Zr or $\text{Al}_3(\text{Zr},\text{Li})$ particles; (d) needle-like precipitates (may be T_1 or Al_2CuLi).



Figure 18. Euler map of left side of weld and base metal.

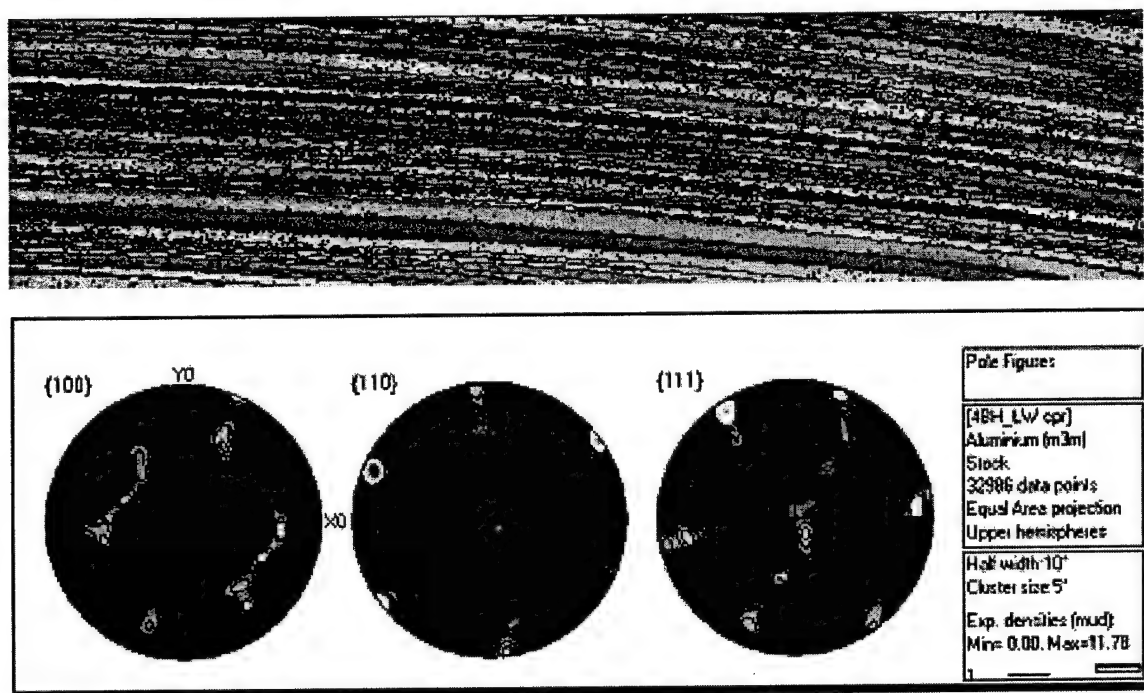


Figure 19. Top: Expanded Euler map of base metal region (shown in Fig. 18); Bottom: Pole figures of base metal region (equivalent to as received rolled plate). Pole figure peak is 11.78.

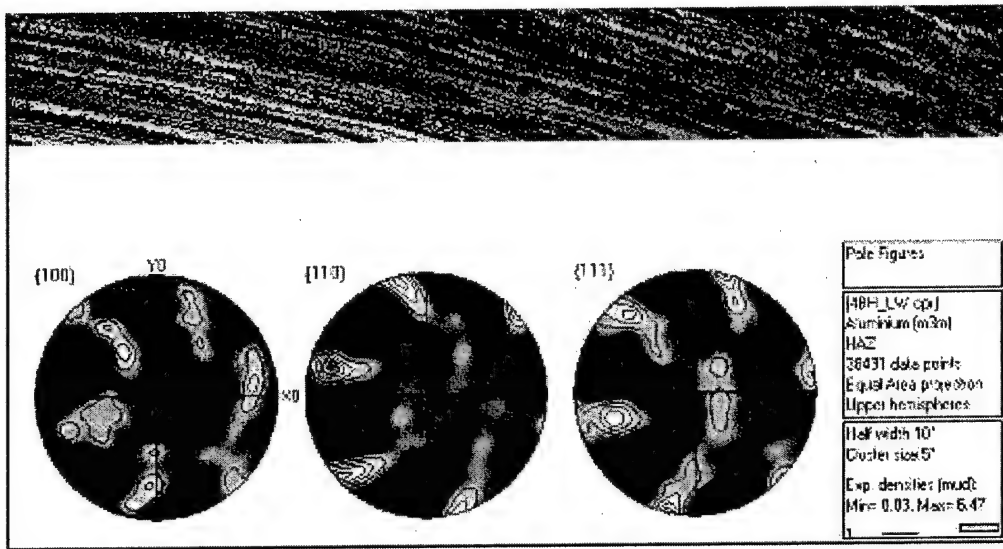


Figure 20. Top: Expanded Euler map of transition region (shown in Fig. 18) from base metal to TMZ/HAZ regions where the grains are rotated by their proximity to the stir zone; Bottom: Pole figures of this transition region.

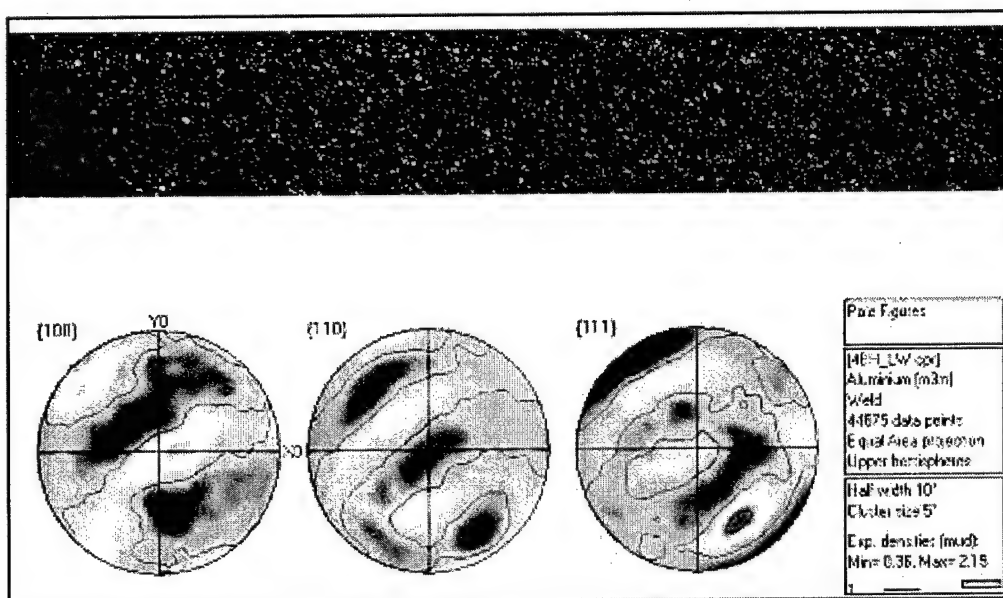


Figure 21. Top: Expanded Euler map of weld nugget DXZ region (shown in Fig. 18); Bottom: Pole figures of weld nugget region.

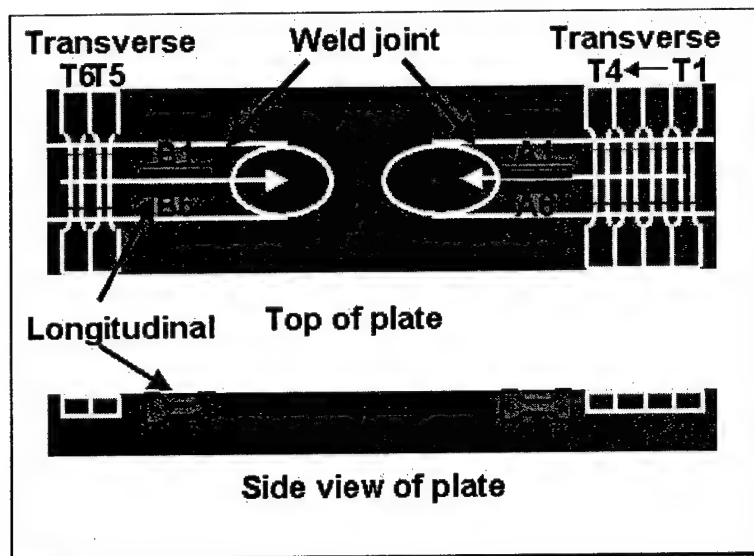


Figure 22. Configurations of transverse and longitudinal tensile specimens relative to the FSW joint .

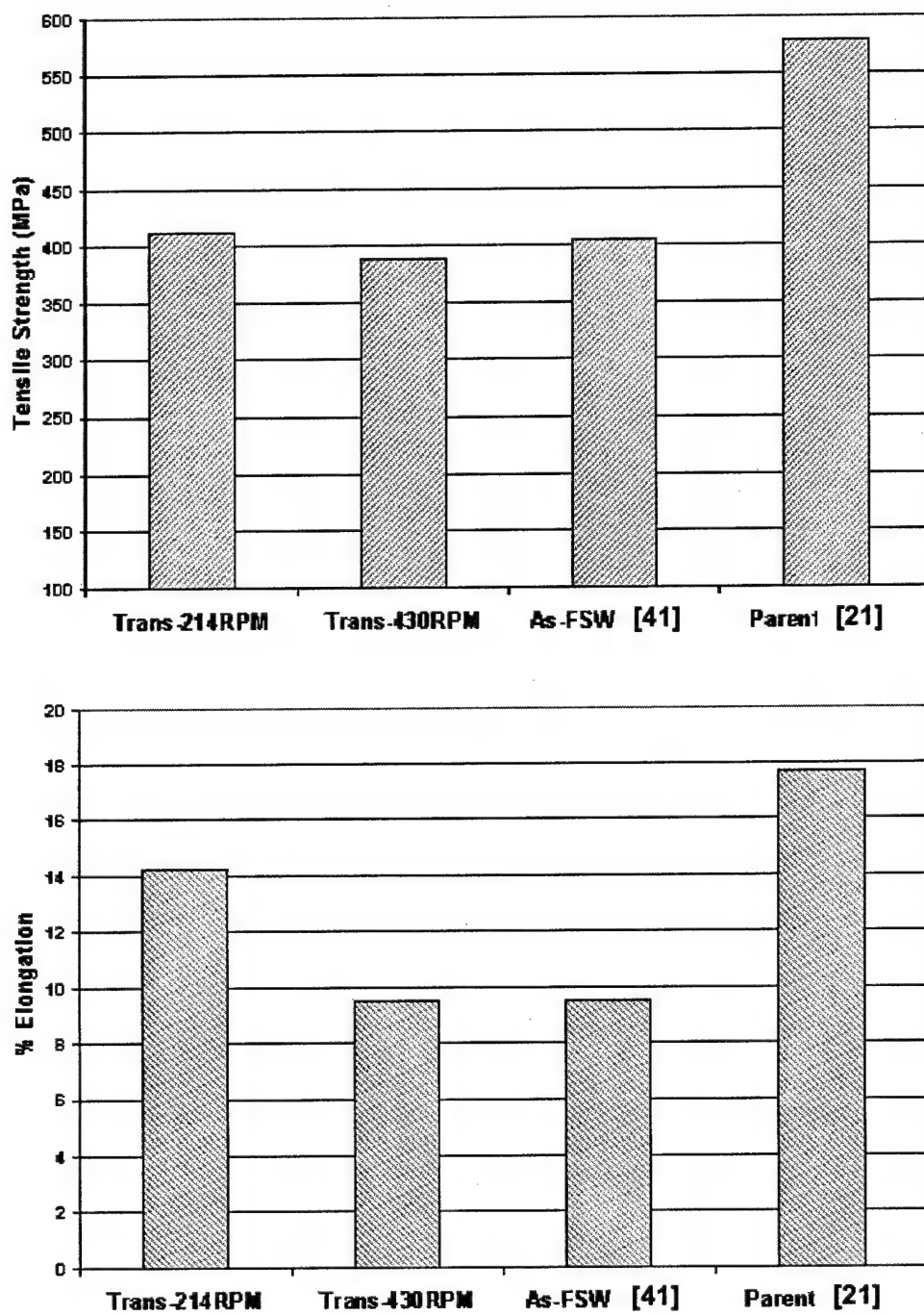
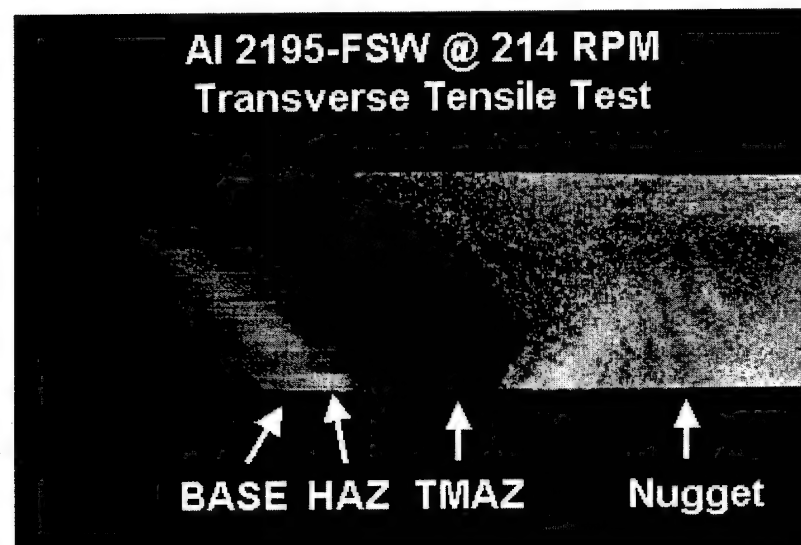
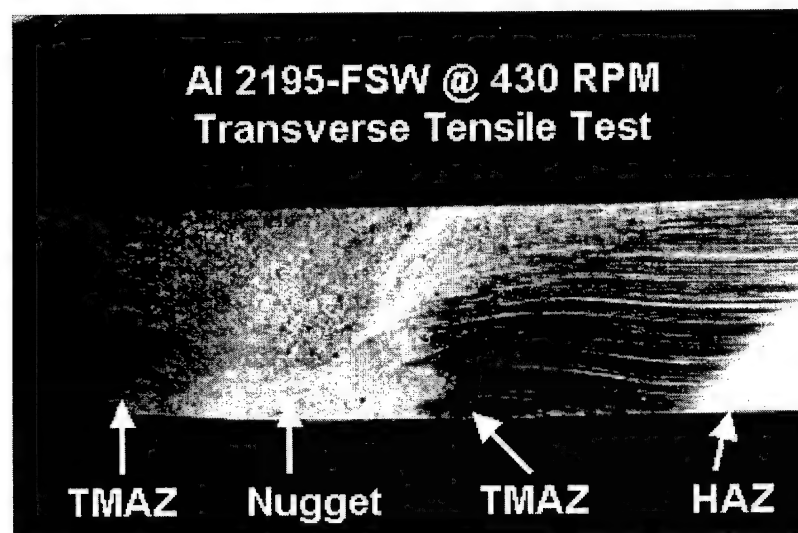


Figure 23. Transverse tensile data for 214- and 430-RPM FSW specimens, compared with data for parent Al 2195 metal from Li et al. [21] and FSW Al 2195 from Arbegast et al. [41]: (a) Tensile strength; (b) % Elongation.



(a)



(b)

Figure 24. Failure location relative to the FS joint in the transverse-tensile-tested specimens (a) 214-RPM and (b) 430-RPM FSW.

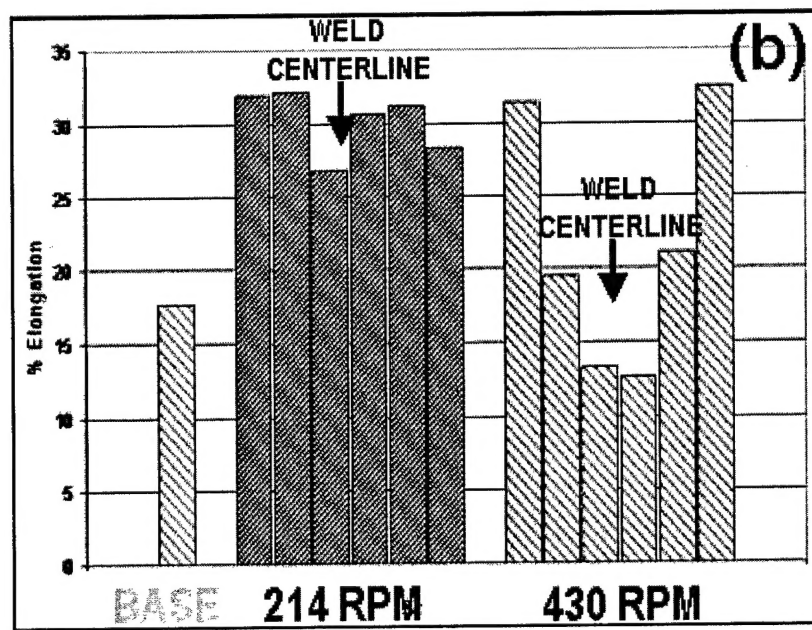
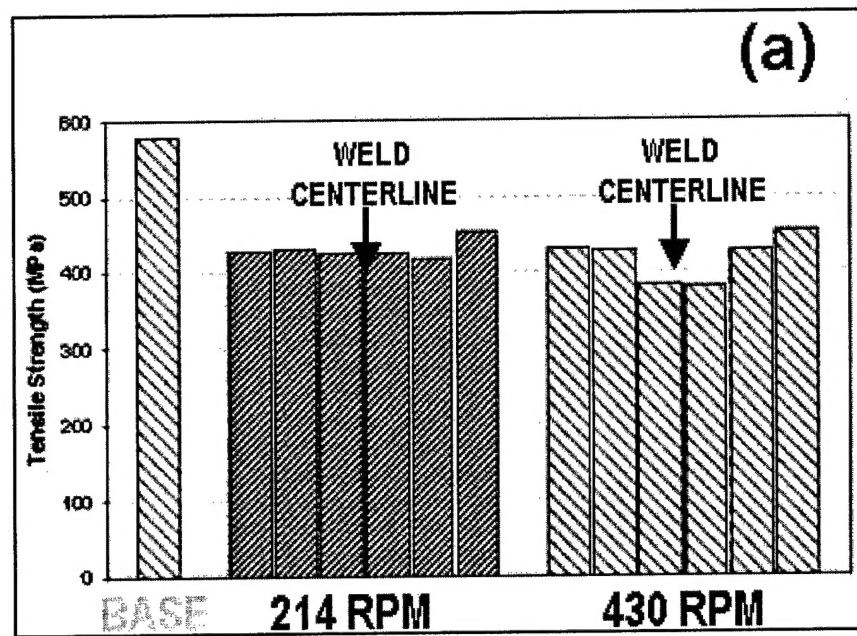


Figure 25. Longitudinal (al-weld metal) tensile data for 214- and 430-RPM FSW specimens, compared with data for parent AA 2195 metal from Li et al. [21]: (a) Tensile strength; (b) % Elongation.

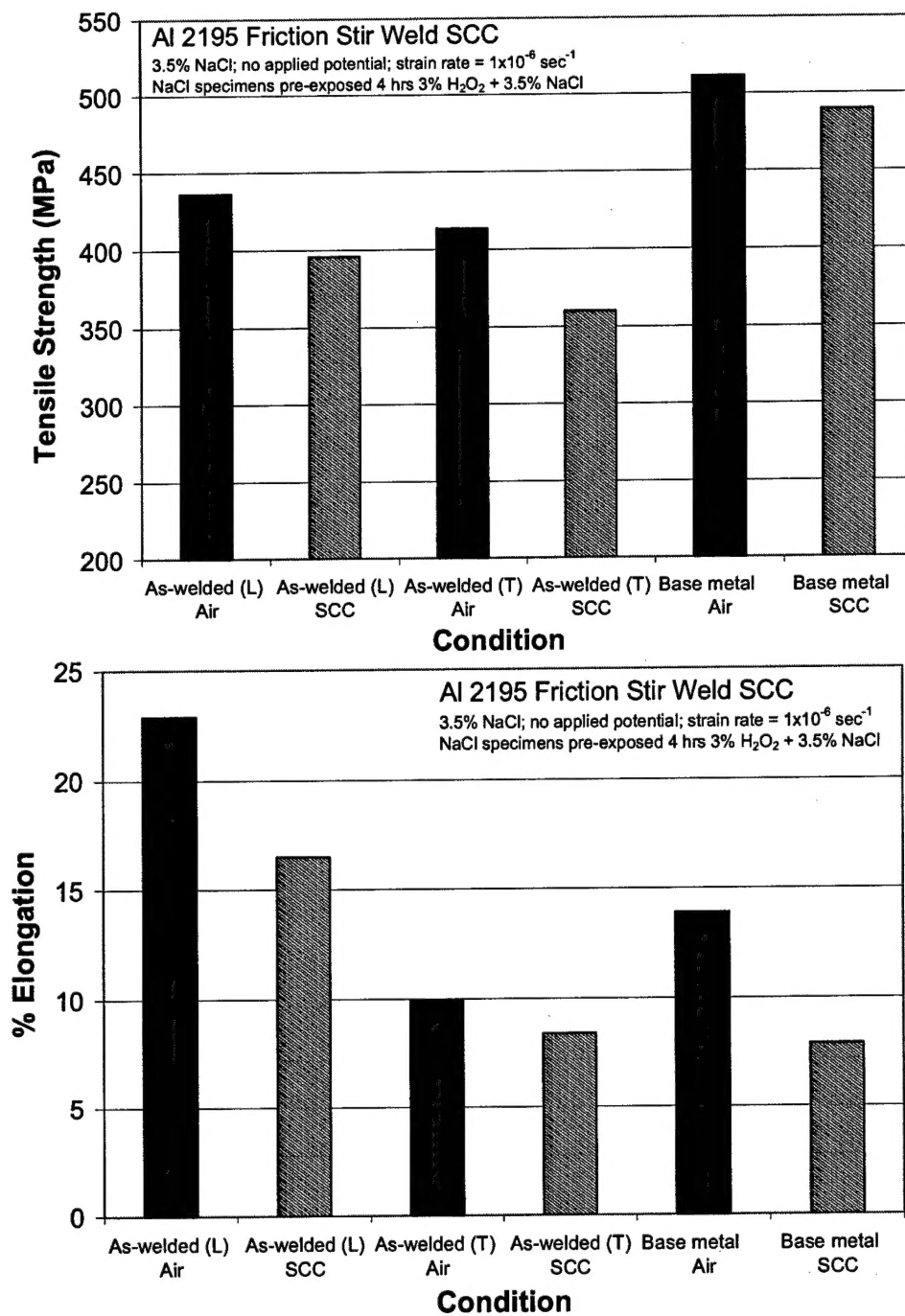


Figure 26. SCC data for 214-RPM FSW specimens compared with results for air and parent Al 2195 material (a) Tensile strength; (b) % Elongation.

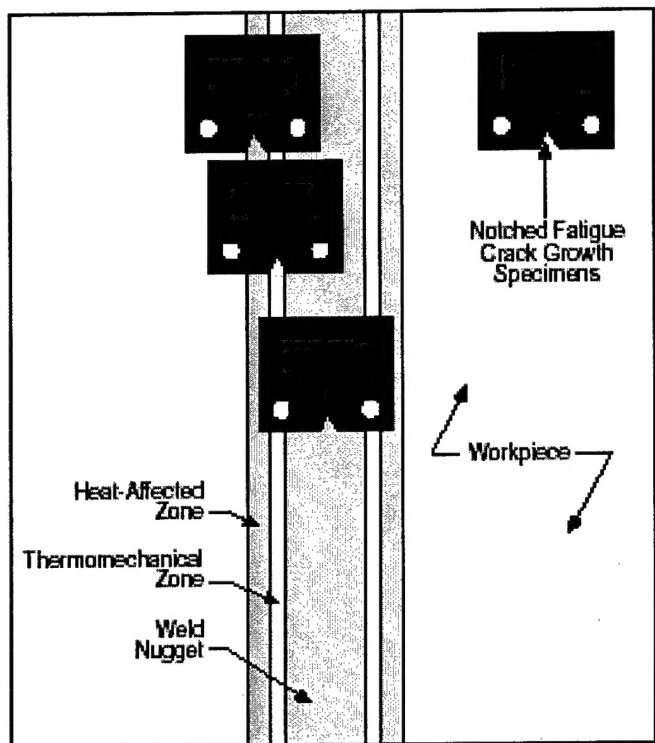


Figure 27. Specimen orientations for fatigue crack testing.

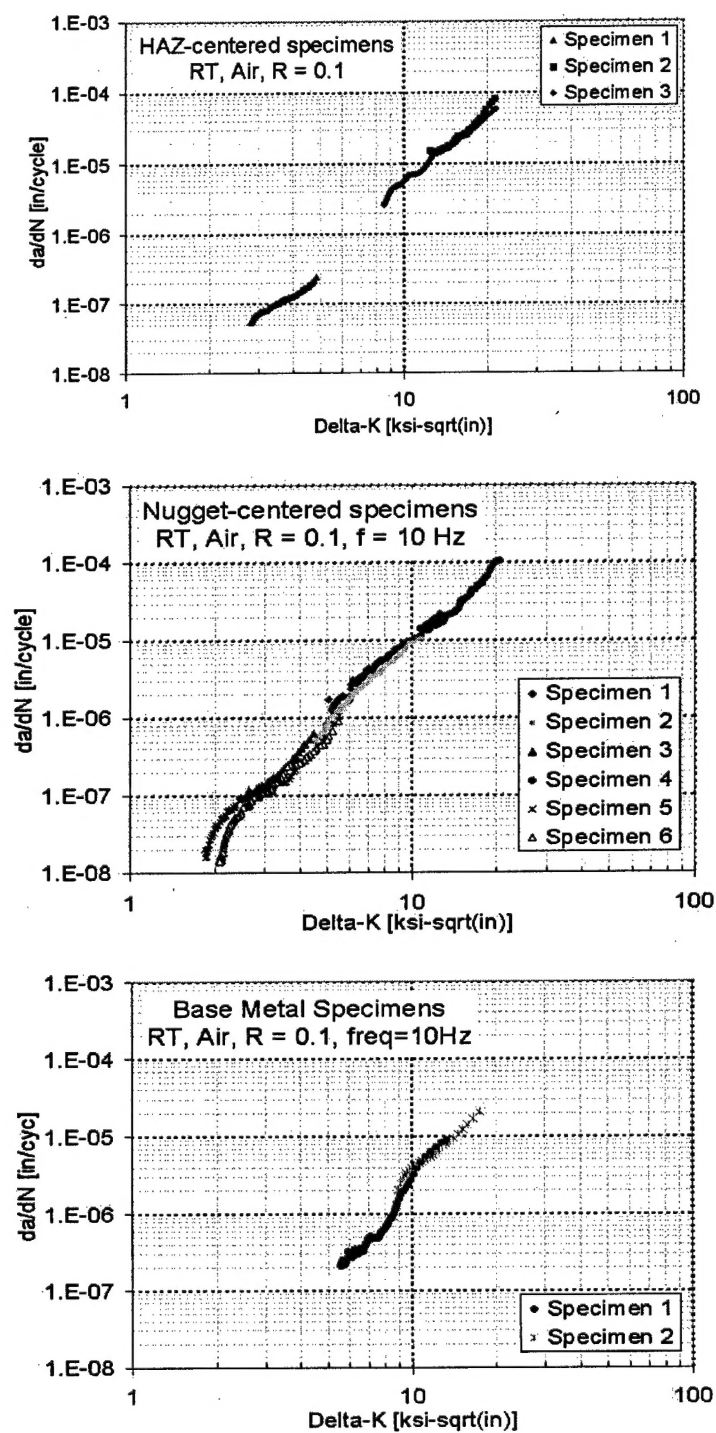


Figure 28. Fatigue crack growth rates (da/dN) vs. cyclic stress intensity (ΔK) in the HAZ and weld nugget regions compared with those in the base metal.